Department of Physics and Astronomy

University of Heidelberg

Master thesis

in Physics

submitted by

Florian Jörg

born in Bretten

2017

Investigation of coating-based radon barriers and studies towards their applicability in liquid xenon detectors

This Master thesis has been carried out by Florian Jörg

at the

Max-Planck-Institut für Kernphysik

under the supervision of

Herrn Prof. Manfred Lindner

Untersuchungen zur Radondurchlässigkeit von Oberflächenbeschichtungen sowie deren Anwendungsmöglichkeit in flüssig Xenon Detektoren

Für gegenwärtige und zukünftige Experimente, die auf die Suche seltener Ereignisse ausgelegt sind, ist die Untergrundreduktion von fundamentaler Bedeutung. Flüssig Xenon Detektoren wie XENON1T, die nach einem direkten Nachweis für dunkle Materie suchen, sind hierfür ein Beispiel. Den größten Beitrag zum Untergrund des XENON1T Detektors leistet die ^{222}Rn Emanation von Detektormaterialien.
Verschiedene Oberflächenbeschichtungen wurden auf deren reduzierenden Einfluss auf die Radonemanation hin bewertet. Das beste Resultat wurde durch die Elektrodeposition von Kupfer erzielt, welche die ^{220}Rn Emanation um zwei Größenordnungen reduzierte. Die ^{222}Rn Emanationsrate wurde in diesem Fall ebensfalls signifikant reduziert. Verschiedene Beschichtungsverfahren, darunter Sputtern, Plasmadeposition und Elektrodeposition, wurden untersucht.
Mithilfe des **He**idelberg **Xe**non Systems, sollen Stabilität und Einfluss der Beschichtungen unter den Einsatzbedingungen in einer Zweiphasen flüssig Xenon TPC getestet werden. Als Vorbereitung hierfür, wurde eine Einphasen Messung mithilfe einer ^{83m}Kr Quelle erfolgreich durchgeführt. Die hierbei erzielten Ergebnisse werden präsentiert.

Investigation of coating-based radon barriers and studies towards their applicability in liquid xenon detectors

For current and future experiments searching for rare events, background control and reduction are of crucial concern. Liquid xenon detectors searching for dark matter such as XENON1T are among these detectors. One of the largest contributions to its background is due to ^{222}Rn emanated from detector materials. Radon mitigating properties of surface coatings applied by plasma deposition, sputtering and electrodeposition were investigated in this work. The most promising result was achieved by the application of an electrodeposited copper coating, which reduced the ^{220}Rn emanation rate by two orders of magnitude. In this case the ^{222}Rn emanation rate also showed a significant reduction.
The impact and stability of the coating layers under operating conditions in a liquid xenon dual phase TPC will be tested in the **He**idelberg **Xe**non system. In preparation for this, data analysis for a first successful calibration of the detector in single-phase mode using a ^{83m}Kr source, are presented.

Contents

1 Introduction to dark matter detection

As recent observations have shown, baryonic matter accounts for less than 5% of the present content of the universe [1]. The dominating contribution to the matter content consists of so called "dark matter". Up to now, its nature remains one of the most important questions in modern cosmology. The XENON1T detector is one of the most sensitive devices aiming to solve this mystery.

1.1 Dark matter and its direct detection

The first speculations about the existence of non luminous matter came up when the observed kinematic of celestial objects did not match the expectation from Newtonian mechanics. Fritz Zwicky was one of the first who reported that the visible mass of the Coma cluster is too small to account for the high velocity dispersion of its galaxies [2]. In 1970 Vera C. Rubin measured the orbital velocity of stars around the center of the Andromeda galaxy. She found that their velocity is not decreasing with their distance from the center as is expected from the Keplerian laws, but stays constant. This discrepancy can be resolved when a halo of dark matter around the galaxy is assumed. Dark refers here to the absence of any electromagnetic interaction, including the emission of photons.

The discovery of the CMB (**C**osmic **M**icrowave **B**ackground) and its imprinted temperature fluctuations, is the foundation for the cosmological Standard Model. This model is able to describe the anisotropies of the CMB temperature with a very high accuracy. It requires that a large fraction of the matter content of the universe is made up by dark matter. Using this model, the actual contribution of dark matter to the total energy density of the universe can be extracted from precise measurement of the temperature fluctuations in the CMB. The most recent values were reported by the Planck collaboration [1], measuring the amount of dark matter to be 25.9% of the energy density of the universe. 69.1% are attributed to dark energy and the residual 5% is baryonic matter, i.e. matter described within the Standard Model of particle physics.

Simulations on the large scale structure of the universe use these density fluctuations as seeds for structure formation. They show that a large scale structure which is compatible with our observations, can be produced by non-relativistic (cold) dark matter [3].

A well motivated class of candidates, fulfilling the requirements demanded from a dark matter particle are WIMPs (**W**eakly **I**nteracting **M**assive **P**articles) [4].

Several examples for such particles would occur naturally in many theories beyond the Standard Model of particle physics. If they were produced thermally in the early universe, their cross section is constrained in order to match the present dark matter density. Coincidentally, the magnitude of the resulting cross section is in the typical range of the weak interaction [5].

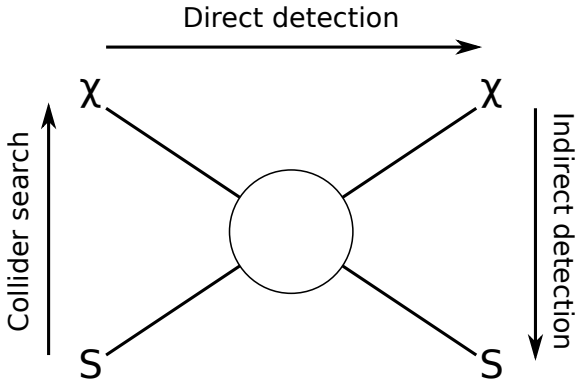

Figure 1.1: Scheme of possible observation channels for interaction of dark matter particles (χ) with Standard Model particles (S).

Since WIMPs couple to ordinary baryonic matter via the weak force, this opens three ways for their detection. In a collider based search, it is attempted to produce dark matter particles by the collision of Standard Model particles. After their creation, dark matter particles will leave the detector undetected, leading to an apparently unbalanced energy momentum conservation in the event [6].
Indirect searches look for the annihilation signal of dark matter particles into particles of the Standard Model. The highest annihilation rate is expected from regions with a high dark matter density, for example the center of galaxies or the Sun [7].

Like all other galaxies, the Milky Way is expected to be embedded into a dark matter halo. A direct detection of the interaction of a WIMP with a nucleus in a detector could therefore be possible. Since the expected interaction rate is very small, extremely low background conditions are required. The developed detectors rely on the detection of phonons, scintillation light and/or ionization induced by the elastic scattering of dark matter with a target nuclei. Liquid xenon detectors gave the strongest limits on the WIMP nucleus cross section for WIMP masses larger than $5\,\mathrm{GeV/c^2}$ [5].

1.2 The XENON1T experiment

The XENON1T detector is an example of a dark matter direct detection experiment. It employs a dual-phase liquid xenon TPC with a length of 1 m and 1 m diameter, having a target mass of about 2.0 tons [8]. In the following, the working principle of

a dual-phase TPC will be described. Then the dominating background sources for dark matter searches with XENON1T are introduced.

1.2.1 Dual-phase liquid xenon time projection chamber

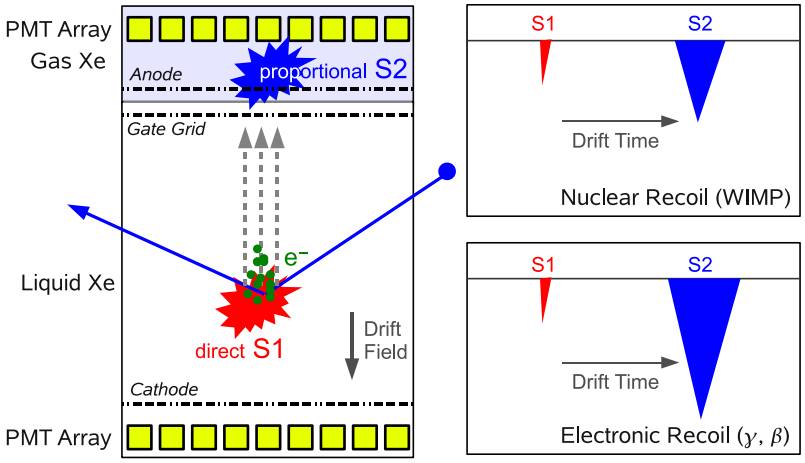

Figure 1.2: Detection principle of a dual phase TPC. Particle interaction produces direct scintillation signal S1 and electrons. Electrons are drifted upwards and get extracted from the liquid into the gas phase, where a light signal S2 is produced by proportional scintillation. The drift time allows to determine the height within the TPC, that the interaction took place. Figure taken from [9].

Figure 1.2 shows the working principle of a dual phase TPC. The detector consists of an active volume, that is partially filled with liquid and gaseous xenon. During operation, the liquid layer is kept at a stable height between an anode and a gate grid. A cathode grid is installed in the lower part of the active volume. **P**hoto**m**ultiplier **T**ubes (PMTs) are installed within two arrays at the bottom of the detector and above the liquid layer of the TPC.

In interactions of particles with the liquid xenon, scintillation light as well as electron-ion pairs (due to ionization) can be produced [9]. The light signal (S1) can be detected by the two PMT arrays. Along the length of the TPC, an electric field is applied between the cathode and the grounded gate grid. Due to the electric field, the electrons that were produced are drifted upwards towards the liquid level. A positive high voltage is applied to the anode, resulting in an electric field ($> 10\,\mathrm{kV/cm}$), in which the electrons get extracted from the liquid phase into the gas phase. By collisions of the electrons with xenon atoms in the gas phase, a second light signal (S2) is produced by proportional scintillation. This second light signal can also be detected by the PMTs. From the distribution of the S2 signal among the individual PMTs in the top PMT array, the x-y position of the initial interaction can be determined. The time difference between the first and second detected light

signal, corresponds to the drift time of the electrons through the liquid xenon. Assuming a constant drift velocity of the electrons, this allows the height in the TPC at which the initial interaction took place, to be determined. Thus, a 3D position reconstruction of interactions is possible.

As illustrated in Figure 1.2 (right), the relative size of the S1 and S2 signal can be used to discriminate between events caused by an electronic recoil (ER) and interactions induced by a nuclear recoil (NR). This enables to discriminate background events (ER) from events, expected to be produced by WIMPs (NR).

1.2.2 Radon induced background in the XENON1T experiment

Since the XENON1T detector searches for very rare interactions of WIMPs with liquid xenon, the reduction of possible background sources is crucial. To shield the detector from cosmic radiation, it is located in the LNGS (**L**aboratori **N**azionale del **G**ran **S**asso) underground laboratory in Italy. Naturally occurring radioactive trace impurities are present in almost all materials used for the construction of the detector. To reduce the background caused by detector materials, they were carefully screened and selected for their radiopurity [11]. Since liquid xenon has a high density of about 3 g/l [5], it efficiently shields against the gamma rays emitted from radio impurities contained in detector materials. By using the aforementioned position reconstruction capabilities of the dual-phase TPC, it is possible to select only the innermost part of the detector for the search. Due to the self shielding of the surrounding liquid xenon, this so called fiducial volume shows a reduced background rate. Besides sources that can cause nuclear recoil events like for example radiogenic neutrons, events due to electronic recoils are an important source of background. Figure 1.3 shows the simulated contributions of different background sources to the electronic recoil rate, as a function of the size of the fiducial volume. It can be seen, that the background induced by detector material increases, as the fiducial mass is increased.

Besides expected background by the elastic scattering of solar neutrinos from electrons in the xenon, Figure 1.3 also shows the expected background contribution caused by the two radioactive noble gas isotopes ^{85}Kr and ^{222}Rn. Since krypton and radon distribute homogeneously within the liquid xenon, this background can not be reduced by fiducialization. The anthropogenic ^{85}Kr can be successfully removed from xenon by cryogenic distillation [12]. For the case of the XENON1T detector, a krypton level of $^{\mathrm{nat}}\mathrm{Kr}/\mathrm{Xe} = 0.36\,\mathrm{ppt}$ was achieved by distillation [13, 14], rendering this background contribution sub dominant.

The remaining and dominating background component in the XENON1T experi-

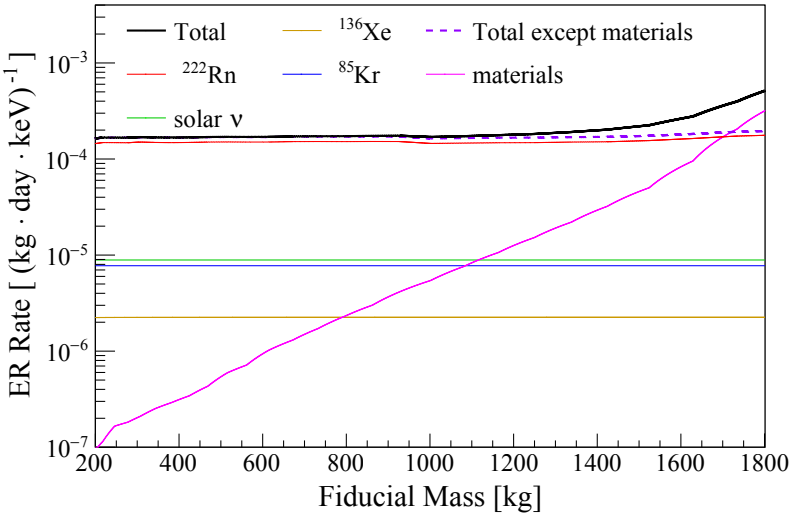

Figure 1.3: Simulated electronic recoil (ER) event rates, introduced by different background components of the XENON1T experiment. The major contribution comes from ^{222}Rn , which is equally distributed in the detection volume. Figure taken from [10].

ment is due to ^{222}Rn [10]. Figure 1.4 shows an excerpt of the ^{238}U decay chain. As can be seen, ^{222}Rn is produced in the decay of ^{226}Ra and has numerous subsequent decays. Especially the beta decays contained in the decay chain are an important background component. Due to the imperfect discrimination between electronic recoil events and nuclear recoil events, they can produce signals that might be mistaken as potential WIMP candidate events. ^{222}Rn mainly originates from the emanation of material surfaces, that are in contact with the xenon. Besides screening and selection of components presenting a low radon emanation rate [17, 18], online removal of radon by cryogenic distillation of xenon can be used to reduce the radon induced background as was proven in [19, 20].

The following chapter will focus on the mechanisms of radon emanation and detection methods that were used in this work. The Investigation of radon mitigating properties of surface coatings will be reported in the third chapter, alongside with the description of the samples and the coating techniques that were used in this study.

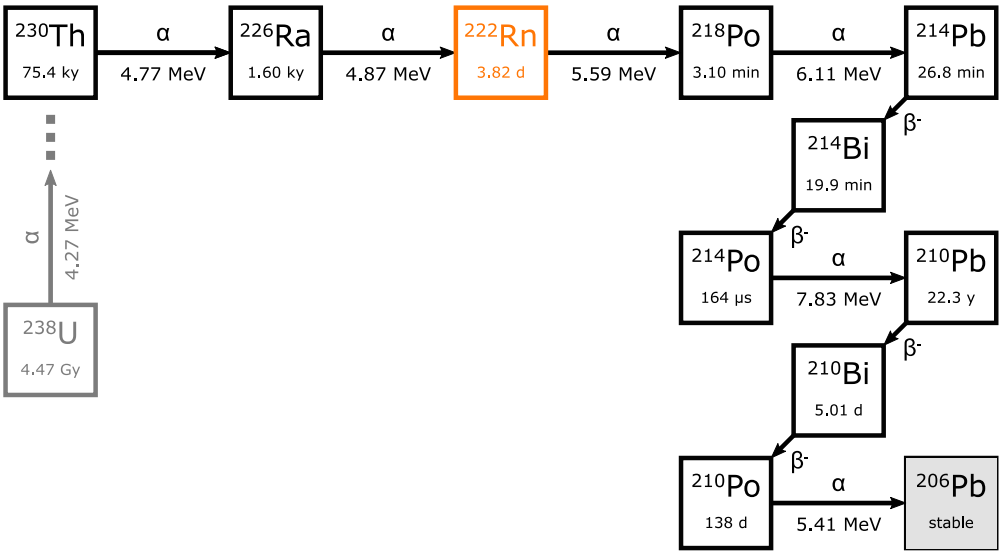

Figure 1.4: Part of the primordial ^{238}U decay chain containing ^{222}Rn . Only containing decays having a significant branching ratio.

2 Radon detection and mitigation

The XENON1T experiment was introduced with its main source of background being due to the emanation of ^{222}Rn from detector materials [10]. The first part of this chapter focuses on the processes that can lead to radon emanation. Afterwards, the measurement techniques to determine the radon emanation rate of the investigated samples will be described.

2.1 Radon emanation

In general, the release of radon from a material surface into the surrounding gas or liquid is referred to as radon emanation. The rate of emanation depends on different material parameters but also on the distribution of the mother isotope ^{226}Ra . There are two possible processes that can lead to the release of radon from the solid phase, which will be described in the following Thereby we consider always the emanation from solid detector materials into surrounding gas or liquid.

2.1.1 Emanation due to diffusion:

The diffusion of radon is driven by the thermal motion of the atoms within a solid. If a radon atom is produced close to the surface of the material, it can diffuse to the material surface before it decays. From the surface, it can then get dissolved by the surrounding gas. The amount of diffusion depends on the concentration gradient as well as on the diffusion constant. A larger diffusion constant usually results in a larger contribution of diffusion to the emanation. The dependence of the diffusion constant D with the temperature T is given by the Arrhenius equation [21]

$$D(T) \propto \exp\left(-\frac{E}{R \cdot T}\right). \tag{2.1}$$

Where R is the universal gas constant and E is a measure for the energy, that is required for a radon atom, to change its lattice position. A diffusion dominated radon emanation is therefore expected to show a strong dependence with the temperature.

2.1.2 Emanation due to recoil:

The alpha particle produced in an alpha decay carries most of the energy that is released in the decay. To conserve energy momentum, however the daughter nucleus

is affected by a recoil directed in the opposite direction of the emerging alpha particle. The kinetic energy $E_{daughter}$ of the produced daughter nucleus is given by [22]

$$E^{kin}_{daughter} = \left(1 - \frac{M_{daughter}}{M_{mother}}\right) Q_\alpha, \tag{2.2}$$

where M_{mother} is the mass number of the mother nuclide, $M_{daughter}$ is the mass number of the daughter nuclide and Q_α is the alpha decay energy. The daughter nucleus looses its energy in collisions within the substrate material. Typically, the nucleus thereby traverses several tens of nm of solid material. If a radon atom is produced close enough to the surface, $E^{kin}_{daughter}$ can be sufficient to eject it through the material surface. Thus the radon atom is emanated.

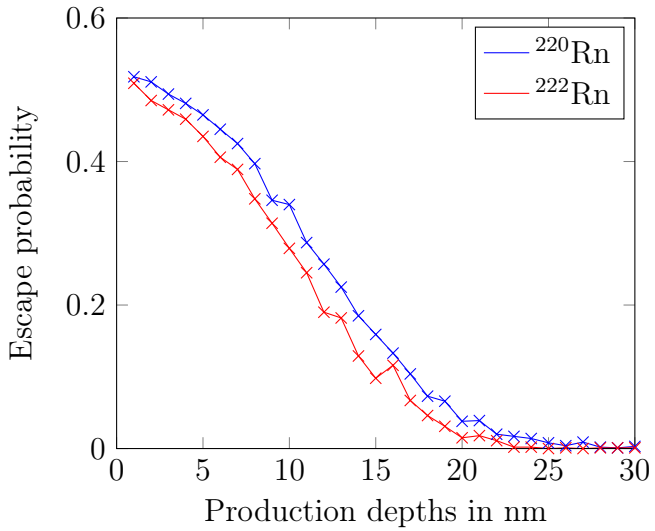

Figure 2.1: Dependence of the escape probability for ^{222}Rn and ^{220}Rn for production at different depths within the material. Simulated using SRIM [23].

Simulation of the range of ions in matter: The range that a radon atom can penetrate before it is stopped in matter, can be computed using the Monte Carlo tool SRIM (**S**topping and **R**ange of **I**ons in **M**atter). It simulates the path of a large number of projectile atoms through the target material, while step wise computing their change in direction and loss of energy due to scattering processes with the target material. Further details on the simulation tool can be found in [23].

SRIM was used to estimate the amount of radon that is able to escape through a material surface by recoil from a preceding alpha decay. Figure 2.1 shows the dependence of the escape probability with the depths at which the radon atom was produced. It compares the emanation fraction for ^{222}Rn and ^{220}Rn . From the simulation it can be seen, that the escape probability approaches a factor of 1/2

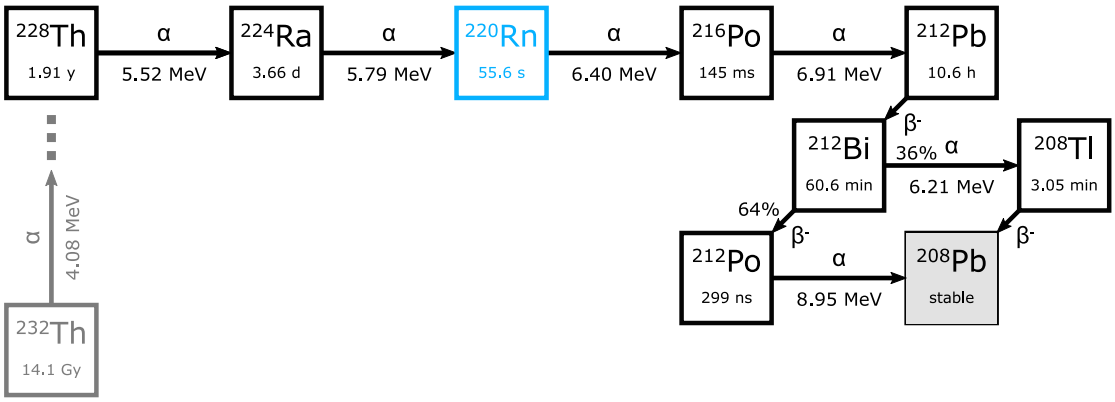

Figure 2.2: Part of the ^{232}Th decay chain containing ^{220}Rn .

if the decay happens very close to the surface. This is expected, since the decay happens isotropic and only radon atoms that are emitted into the upper half of the solid angle can possibly escape. It is also visible that the escape probability for ^{220}Rn is usually higher, than the one for ^{222}Rn . This is caused by the 20% higher recoil energy of ^{220}Rn (see Figure 2.2).

2.2 Measurement techniques

Sensitive radon detectors are needed in order to analyze radon mitigation by surface coatings. To determine the mitigation efficiency of an applied coating layer the usual procedure involved the measurement of the radon emanation rate of the sample before and after coating. In the following section two detectors will be introduced which have been employed during this work.

2.2.1 Miniaturized proportional counters

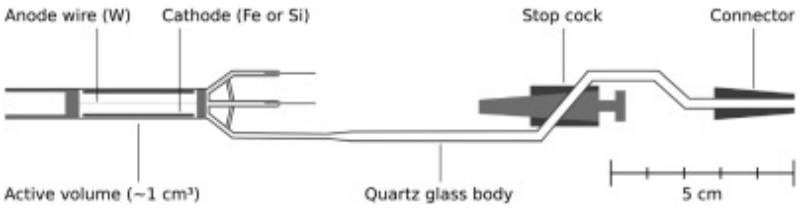

Figure 2.3: Scheme of the miniaturized proportional counters used for ^{222}Rn measurement. Figure taken from [24].

Miniaturized proportional counters were originally developed for the GALLEX solar neutrino experiment [25]. Their minimal detectable ^{222}Rn activity is about 40 μBq [26]. Within the XENON collaboration, the miniaturized proportional coun-

ters are used for material screening with regard to ^{222}Rn emanation [17, 18].

In preparation of a measurement, the sample is stored in a vacuum tight emanation vessel, usually filled with helium as a carrier gas. During this time, the ^{222}Rn activity in the vessel increases due to the emanation from the sample, until an equilibrium is reached after several half-lifes of ^{222}Rn. The radon that is contained in the vessel is extracted and filled together with a counting gas into the miniaturized proportional counter, where the activity is measured.

2.2.2 Radon monitor using electrostatic collection

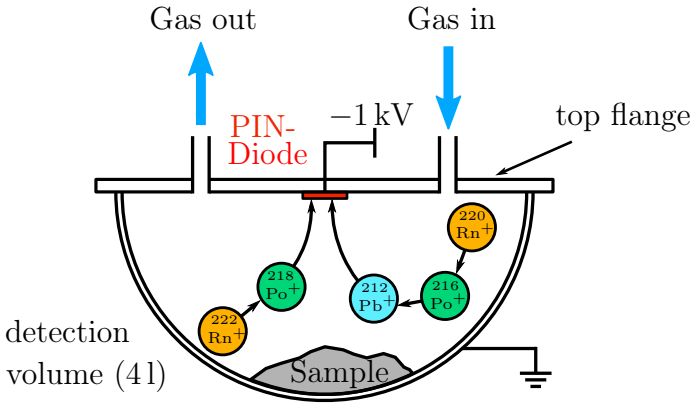

Figure 2.4: Sketch of the working principle of the radon monitor. Radon daughters are produced preferably positively charged and are drifted to the negatively biased PIN diode.

Besides the measurement of the ^{222}Rn emanation rate determination of the ^{220}Rn emanation is of interested for the later discussion of radon mitigation. ^{220}Rn is part of the decay chain of ^{232}Th , that is depicted in Figure 2.2. Since the radon monitor is able to also detect the emanation of ^{220}Rn , it was mainly used for this study.

The monitor consists of a hemispherical stainless steel bowl, with a volume of about 4 l. A Teflon socket holding a (windowless) silicon PIN diode is mounted to the top flange that closes the detector. Two ports for gas in and outlet are also attached on the top flange. A sketch showing the main components of the monitor is shown in Figure 2.4.

For a measurement of the radon emanation rate, the samples are placed directly inside the bowl of the detector. The detector is then filled with nitrogen to an operating pressure of about 1050 mbar. Radon that is emanated from the sample, decays within the monitor. It was shown that most radon daughters that are produced by alpha decay carry a positive charge [27]. The detector maintains an electric drift

field between the grounded steel vessel and the PIN diode to which a negative high-voltage of −1000 V is applied. This leads to a collection of the radon decay products on the surface of the diode [28].

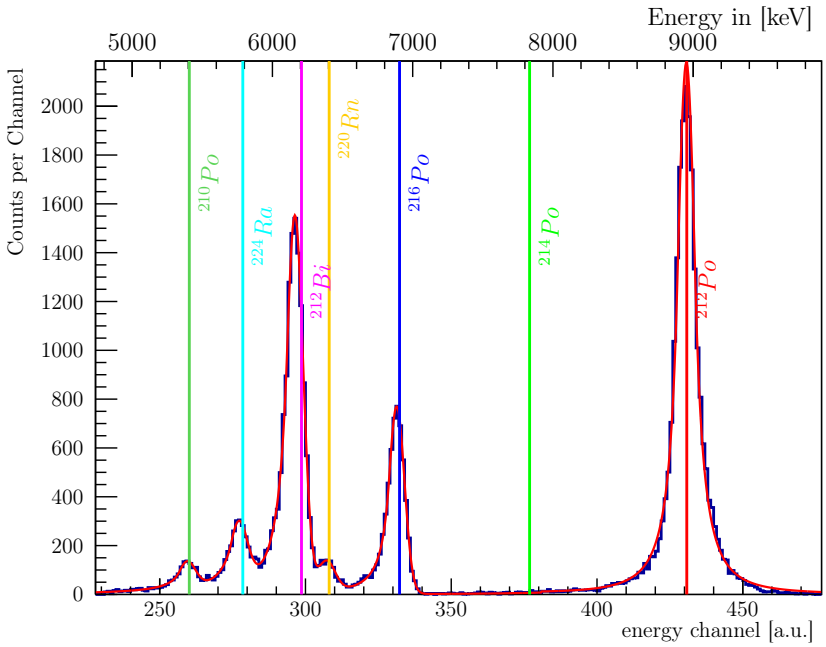

Figure 2.5: Energy spectrum as recorded with the radon monitor using a ^{220}Rn source. The colored lines correspond to the literature values of the respective alpha decays. A sum of cristal ball functions is fitted to the spectrum (see Text).

Alpha particles produced in the subsequent decays, that are directed towards the PIN diode, will produce electron/hole pairs within the silicon substrate. The charge signals from these decays are then amplified and translated into a digital signal. According to the amount of charge, that was detected, an energy channel in the range of 0 to 1000 is assigned. Since the amount of charge is proportional to the energy of the alpha particle, the channels correspond to distinct energies. A typical energy spectrum of a ^{232}Th source is depicted in Figure 2.5. The peaks of all alpha decays, that are part of the ^{220}Rn decay chain are visible[1]. The shape of most peaks show a Gaussian part on the right hand side of the mean value as well as a pronounced tailing towards lower energies. They can be described using the Crystal-ball function [29]:

$$f(E;\mu,\alpha,n,\sigma) = N \cdot \begin{cases} A \cdot \left(B - \frac{E-\mu}{\sigma}\right)^{-n}, & \text{for } \frac{\mathrm{E}-\mu}{\sigma} \leq -\alpha \\ \exp\left(-\frac{(E-\mu)^2}{2\sigma^2}\right), & \text{for } \frac{\mathrm{E}-\mu}{\sigma} > -\alpha \end{cases} \tag{2.3}$$

[1]The peak of ^{210}Po is visible due to a residual activity of ^{210}Pb, that is sticking on the diode.

where

$$A = \left(\frac{n}{|a|}\right)^n \cdot \exp\left(-\frac{|\alpha|^2}{2}\right),$$
$$B = \frac{n}{|\alpha|} - |\alpha|,$$

and (μ, α, n, σ) are parameters describing the shape of the peak. N is a normalization factor, that can be used to extract the area of the single peak from the fit [29]. The peak of ^{212}Po has a different shape as compared to the other peaks in the spectrum. This is caused by the coincidence counting of the preceding beta decay of ^{212}Bi . Due to the very short half-life of ^{212}Po, these two decays can not be resolved separately. Since the energy of the electron emitted in this decay can not be completely contained in the diode, an additional tailing towards higher energies is visible. In order to describe this peak shape, a symmetric Crystal-Ball function was defined as follows:

$$f(E;\mu,\alpha,n,\sigma) = N \cdot \begin{cases} A \cdot \left(B - \frac{E-\mu}{\sigma}\right)^{-n}, & \text{for } \frac{\mathrm{E}-\mu}{\sigma} \leq -\alpha \\ \exp\left(-\frac{(E-\mu)^2}{2\sigma^2}\right), & \text{for } \frac{\mathrm{E}-\mu}{\sigma} > -\alpha \text{ and } \frac{\mathrm{E}-\mu}{\sigma} < +\alpha \\ A \cdot \left(B - \frac{E+\mu}{\sigma}\right)^{-n}, & \text{for } \frac{\mathrm{E}-\mu}{\sigma} \geq +\alpha \end{cases} \tag{2.4}$$

In order to fit the entire spectrum (Figure 2.5) the two sided Crystal-Ball function Eq. 2.4 for the ^{212}Po peak is combined with the sum of five other Crystal-Ball functions (Eq. 2.3) for the other peaks. Doing so it is possible, to obtain the activities detected for each isotope even though their spectral peaks overlap. Also, the mean values of the decay energies are retrieved from the fit, which are then used for detector calibration.

For all isotopes, fitted in the spectrum, the mean value deduced from the fit function can be plotted versus the literature value of their alpha decay energy Q_α. Figure 2.6 shows the result of such a calibration plot with the fitted linear conversion function that can then be used to assing each channel a corresponding energy value. The linearity of the detector in the investigated energy range is very good.

Similarly as done in [30], the ^{212}Po peak can be used to determine the ^{220}Rn emanation rate. To do so it is necessary to take the correct time evolution of the ^{212}Po activity into account. As can be seen from the decay chain (Figure 2.2), ^{212}Po is formed via the decay of ^{212}Pb , which has a prolonged half-life of $T_{1/2} = 10.6\,\mathrm{hrs}$. Thus, the ^{212}Po activity shows the typical in growth behavior shown in Figure 2.7. The analytic function, used to derive the equilibrium activity by fitting it to the data was reported in [30] and is given in Appendix A.

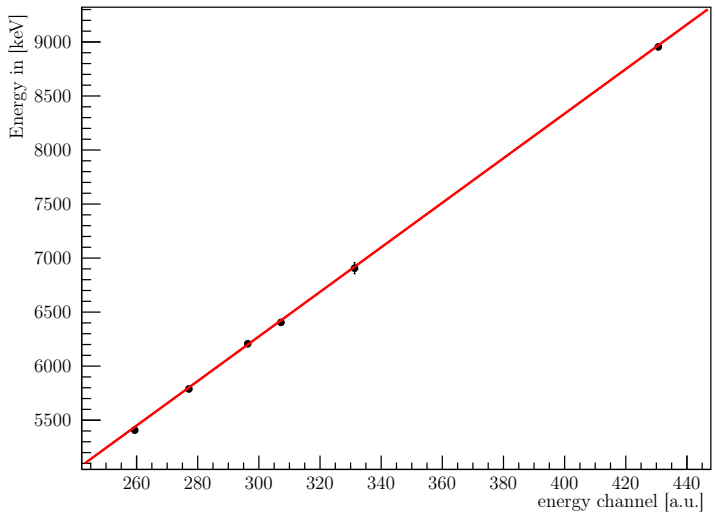

Figure 2.6: Mean values of all spectral peaks from the above example plotted against their theoretical decay energy. A linear function describes the relation reasonably well. Most of the error bars are smaller than the marker size.

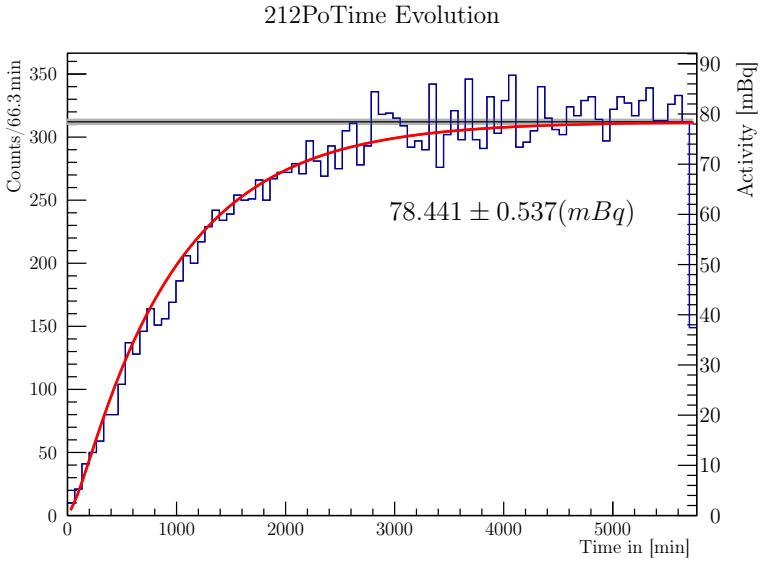

Figure 2.7: The time evolution of the ^{212}Po activity. The growing in is well described by the function reported in [30].

3 Study of surface coating for radon mitigation

This chapter presents results on the reduction of radon emanation by the application of surface coatings. Previously published results on the reduction of ^{220}Rn emanation [30] could be confirmed. Further investigations, on the impact of coating thickness and temperature on radon mitigation with simultaneously employing different coating techniques are discussed in this work.

3.1 Samples for radon emanation studies

Current and future low background experiments, like XENON1T, depend on stainless steel for the construction of detector components. Investigation of radon mitigation by coating layers on stainless steel samples therefore is of interest. However stainless steel usually contains low amounts of radio-impurities [11, 31], which are too close to the detection sensitivity of the available devices. Therefore alternative samples such as thoriated welding rods and samples produced by implantation, were used in this work.

3.1.1 Thoriated tungsten welding rods

Tungsten rods containing thorium-oxide (WTh) have proven to be a source of ^{220}Rn emanation [30]. They are mainly used as electrodes for arc welding and make an appropriate source to investigate the radon reduction of coating layers.

For this study, 17.5 cm long welding rods containing 4% of ThO_2 with diameters of 1 mm and 4.8 mm were investigated (see Figure 3.1). Besides their availability and sufficient ^{220}Rn emanation, these samples come along with two limitations. Since they are made from tungsten, coating layers might behave differently regarding their adhesion and thermal stability when applied to stainless steel. The investigated coating techniques however, are also applicable for samples having a stainless steel surface.

The other limitation of WTh welding rods is the emanation of ^{220}Rn instead of ^{222}Rn, which is the radon isotope that should be primarily addressed by this study. Due to the large difference regarding their half-life, their emanation behavior within coating layers might be different.

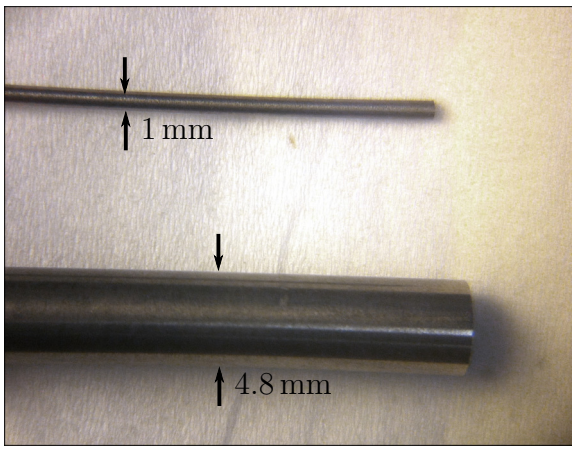

Figure 3.1: Thoriated tungsten welding rods containing 4% ThO_2 with 1 mm and 4.8 mm diameter and a length of 17.5 cm.

It was found, that WTh welding rods also provide a small fraction of ^{222}Rn emanation [33]. Table 3.1 shows the mean amount of ^{222}Rn emanation of these rods as measured with miniaturized proportional counters. Also shown is the mean detected activity in ^{212}Po, determined by the radon monitor. As being part of the ^{220}Rn decay chain, the ^{212}Po activity directly depends on the ^{220}Rn emanation of the sample. Due to the lack of a standard source with known ^{220}Rn emanation, it was not possible to determine the detection efficiency of the radon monitor for ^{220}Rn. However, for the here discussed radon mitigation study only relative changes of the ^{212}Po activity before and after coating are relevant.

The activities, shown in Table 3.1 are averages over several samples, where each sample was measured multiple times. During this study, most of the samples showed an activity, that is compatible with these averages.

Table 3.1: Mean radon emanation of tungsten electrodes containint 4% of ThO_2 with different diameter. ^{222}Rn activities as determined with miniaturized proportional counters. The ^{212}Po activities were measured with the radon monitor. Shown values are averages over several samples, with multiple measurements per sample.

Diameter	N_{rods}	$A(^{222}\text{Rn})$	$A(^{212}\text{Po})$
1 mm	1	$(42.82 \pm 2.02)\,\mu$Bq	(6.98 ± 0.02) mBq
4.8 mm	1	$(65.62 \pm 2.08)\,\mu$Bq	(13.05 ± 0.07) mBq

3.1.2 Implantation of radioactive isotopes with ion beams

A radon emanating sample might be produced by implantation of radium isotopes underneath its surface. In the following, the implantation procedure will be de-

scribed, and first results will be shown.

Implantation of ^{226}Ra at ISOLDE Implanted ^{226}Ra lead to a constant production of ^{222}Rn within the substrate. The total number of ^{226}Ra atoms $N_{226\mathrm{Ra}}$, necessary to be implanted into a sample to produce an activity $A_{222\mathrm{Rn}}$ in ^{222}Rn, can be estimated as follows.

$$\begin{aligned} N_{226\mathrm{Ra}} &= \frac{1}{\lambda_{226\mathrm{Ra}}} \cdot A_{222\mathrm{Rn}} \\ &= \frac{T_{1/2,226\mathrm{Ra}}}{\ln 2} \cdot A_{222\mathrm{Rn}} \end{aligned} \tag{3.1}$$

Where $\lambda_{226\mathrm{Ra}}$ and $T_{1/2,226\mathrm{Ra}}$ are the decay constant and the half-life of ^{226}Ra respectively.

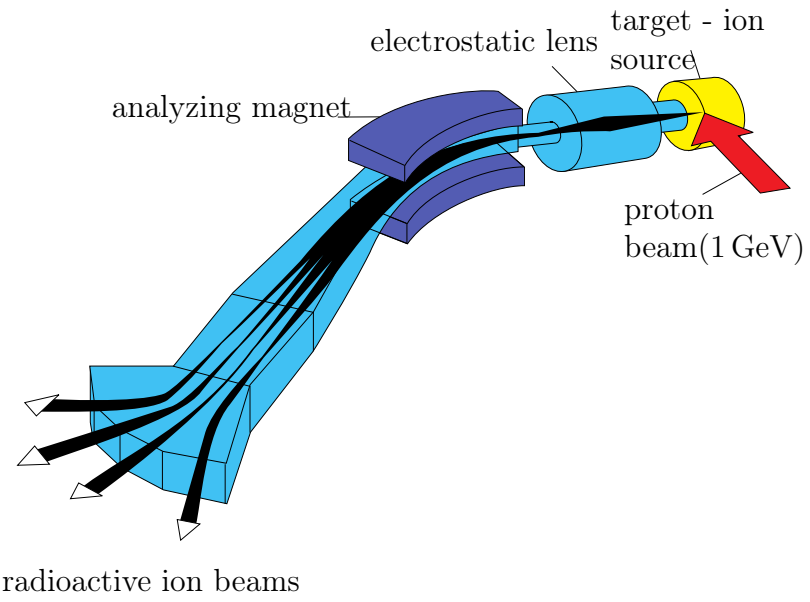

Figure 3.2: Overview of the ISOLDE facility at CERN. Radioactive ions like ^{226}Ra can be produced, separated and implanted. [34]

In this work, two stainless steel samples were produced in cooperation with the ISOLDE (**I**on **S**eparation **O**n**L**ine **DE**vice) facility at CERN. Each of the samples got implanted with about 5×10^{11} ions. By Equation 3.1, the resulting radium activity in each sample can be calculated to be 6.87 Bq. However, as argued in 2.1.2 by geometrical consideration, the maximum amount of ^{222}Rn emanation that can be expected from each sample should be close to 1/2 of this activity.

Figure 3.2 sketches the production and separation of a RIB (**R**adioactive **I**on **B**eam). ^{226}Ra atoms can be produced by irradiation of a depleted ^{238}U target

with 1 GeV protons [35][1]. By heating the target, they are then released from the target surface via diffusion [37]. Not only ^{226}Ra, but also various other isotopes get produced within the target. To get a beam mainly containing the desired isotope, it is necessary to ionize the isotopes from the surface of the target in order to get them accelerated an separated. The ionization source, that was used for the implantation, consisted of a heated tungsten cavity installed close to the target. Since radium is an alkaline earth metal, it can efficiently be ionized by contact with the hot tungsten surface [34]. The ionized isotopes were then accelerated by an electric potential of about 30 kV. Separation was achieved by application of a magnetic field. By this the ions were forced on a circular trajectory where the radius is dependent on the ion's mass to charge ratio.

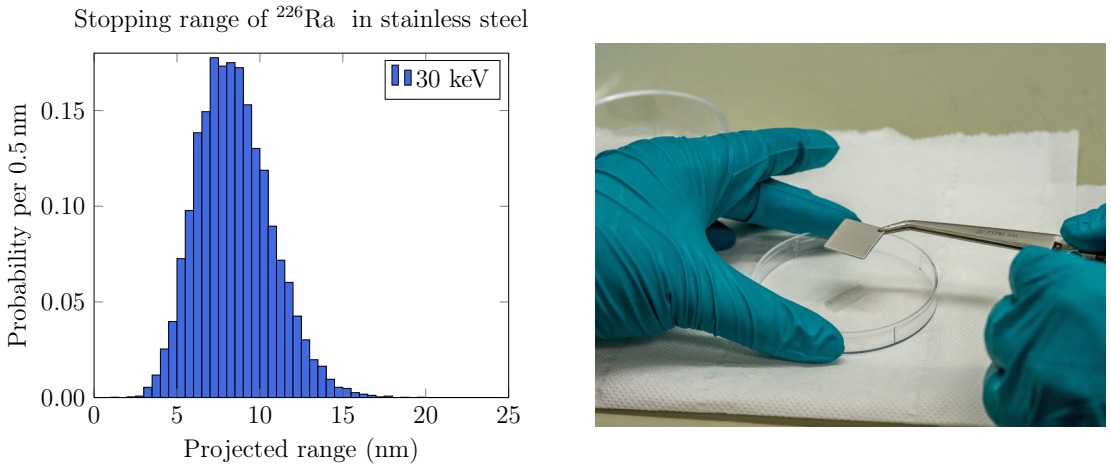

Figure 3.3: **Left:** Expected implantation depth profile of ^{226}Ra ions with an energy of 30 kV into stainless steel. Simulated using SRIM [23]. **Right:** One of the ^{226}Ra implanted samples during preparation for gamma spectrometry. Photograph courtesy of Ralf Lackner.

The separated ion beam is then directed onto the surface of the sample, which is placed in the implantation chamber. Incident ions subsequently loose their kinetic energy by collisions with the atoms of the sample and get implanted underneath the surface. Implantation was done into square samples made from electro-polished stainless steel (X6CrNiMoTi 17-12-2 [31]) with a width of 2 cm and a thickness of 2 mm (see Figure 3.3). During the implantation, the ion beam was swept in order to cover an area of about 5 mm by 5 mm around the center of the sample surface. The depth profile of the implantation was estimated using SRIM (see Section 2.1.2) and is shown in Figure 3.3. The mean implantation depth, that can be expected is 8.47 nm with a standard deviation of 2.24 nm from the mean.

[1] An alternative might be the production of ^{226}Fr in a thorium-carbide target[36]. ^{226}Fr will then decay within $T_{1/2} = 55$ s into ^{226}Ra

Results and Outlook Two weeks after the implantation took place, a gamma spectrometry was performed at CERN, where both samples were measured together. The result from this measurement is summarized in Table 3.2.

Table 3.2: Activities of the samples implanted at ISOLDE as detected by gamma spectroscopy. If not reported, the activities of subsequent decay chain products were found to be in equilibrium. Reported errors represent $\pm 1\sigma$ intervals.

No.	Chain				
	^{225}Ra	^{223}Ra	^{226}Th	^{232}Th	^{226}Ra [a]
1[b]	(5.0 ± 1.7) kBq	(24 ± 2.4) Bq	(50 ± 17) Bq	(34 ± 2.0) Bq	(24 ± 5.0) Bq

[a] Daughters in equilibrium up to ^{210}Pb .
[b] Measurement performed at CERN on 2017-10-11. Both samples were measured at the same time.

It can be seen, that the sample contains an activity of about 24 Bq in ^{226}Ra . This should make the samples good candidates for radon emanation studies in the future. It is also clearly visible, that the samples not only contain ^{226}Ra, but also contributions from other radium isotopes, as well as from other chemical elements. The high activity found in ^{225}Ra is expected to decay with a half-life of 14.9 days. It is expected, that these contaminations do not affect the usability of the sample.

A way to possibly reduce the amount of impurities in a future sample would be the use of an ionization source providing a higher selectivity. For this the laser ionization source RILIS (**R**esonance **I**onization **L**aser **I**on **S**ource) is available at ISOLDE [38]. In order to reduce the contributions from isotopes of different mass numbers in the sample, the HRS (**H**igh **R**esolution **S**eparator) providing a higher mass resolution [39] could be used. To produce a sample that is as close as possible to a realistic case of a homogeneous contamination with radium, it might be necessary to aim for a deeper implantation. This can be done by increasing the energy of the incident ions. At REX-ISOLDE it is possible to post accelerate ^{226}Ra ions up to a total energy of 678 MeV [37]. The increased energy would lead to an implantation of the ions which is expected to be about three orders of magnitude deeper.

Alternatively implantation of radium ions can be achieved by using the recoil energy from a preceding alpha decay. The next section will report results of two measurements suggesting a successful implantation of ^{224}Ra by the decay of ^{228}Th .

3.1.3 Implantation by nuclear recoil

As described in Section 2.1.2 the recoil energy that a nucleus gains by an alpha decay is sufficient to have it traversing a certain amount of matter. Typical energies

of alpha decays are in the region of several MeV. By equation 2.2 this leads to recoil energies for the radium daughters in the range of several tens of keV. This is close to the implantation energies accessible at ISOLDE.

Compared to an implantation using an ion beam, implantation by recoil is expected to lead to a changed implantation depth distribution. Since daughter nuclei are emitted isotropic from the source, their incident angle is not always rectangular to the sample surface. Thus they will stop on more shallow depths on average. Depending on the depth of emission from within the source, the recoiling nuclei loose part of their energy by interactions within the source material. This also leads to less deep distribution of ions within the target.

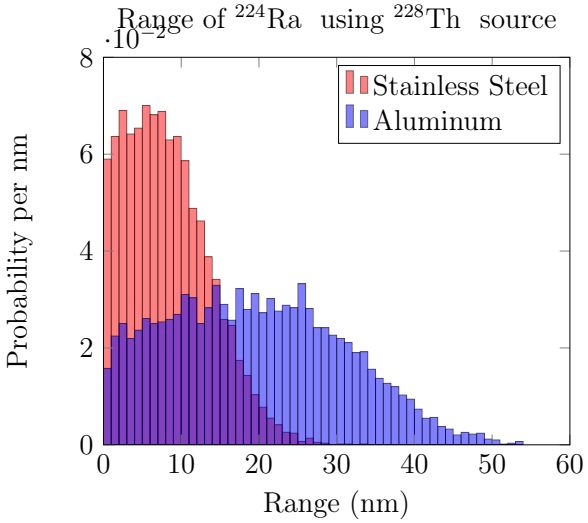

Figure 3.4: Expected depth profile for ^{224}Ra implantation by recoil from a ^{228}Th source into stainless steel and aluminum targets. Simulation done using SRIM [23].

The recoil energy of the ^{224}Ra nucleus produced in the alpha decay from ^{228}Th is given by equation 2.2 and amounts to 96.84 keV. Figure 3.4 compares the expected ^{224}Ra depth profiles for implantation by recoil from ^{228}Th decay into an aluminum and a stainless steel target. It can be seen that implantation into aluminum is expected significantly deeper into the substrate as is the case for implantation into stainless steel.

The ^{224}Ra activity $A(^{224}\text{Ra})$ implanted in the sample should be described by the following ingrowth-law.

$$A(^{224}\text{Ra}) = A_{eq}\left(1 - e^{-\lambda t_i}\right) \tag{3.2}$$

Where λ is the decay constant of ^{224}Ra and t_i is the duration of the implantation

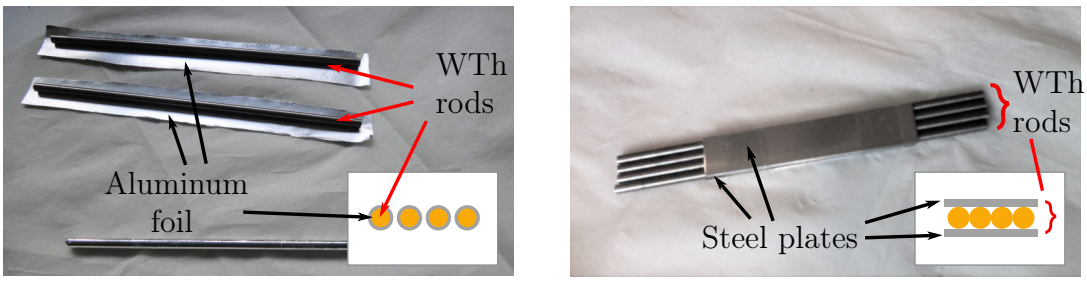

Figure 3.5: **Left:** Aluminum foil stripes wrapped around WTh welding rods to implant ^{224}Ra by recoil (IMP0). **Right:** Image of the implantation assembly for the stainless steel plates (IMP1).

process. A_{eq} is the equilibrium activity in ^{224}Ra that will be approached.

Implantation of ^{224}Ra using thoriated welding rods Two different measurements were done suggesting a successful implantation of ^{224}Ra by this mechanism. In both cases, four thoriated welding rods were used as a ^{228}Th source (see section 3.1.1). For the first test, implantation took place into four aluminum foil stripes, tightly wrapped around each rod, covering the whole circumference and a length of 14.8 cm. This sample will be referred to as "IMP0" (see Figure 3.5, left). The second implantation was done into two rectangular stainless steel plates (X2CrNiMo 18-14-3) with a length of 10 cm, a width of 2 cm and a thickness of 1 mm. The plates were fixed lying flat above and below the four rods (see Figure 3.5, right). This sample will be referred to as "IMP1". Both samples were cleaned from grease prior to the implantation. Before storing the sample in a sub millibar vacuum for the implantation, the implantation vessel was flushed with nitrogen. The duration and results of both implantations are summarized in Table 3.3.

After the implantation the samples were cleaned to remove any potential surface contamination caused by thorium containing dust. The implanted sides of the aluminum foil stripes were thoroughly wiped with iso-propanol and lab tissues. For the stainless steel plates it was decided to investigate if the implanted radium gets dissolved in a solution of copper sulfate and sulfuric acid. Prior to submersion into the 40 °C warm bath, they were sprayed with pressurized, de-ionized water. After cleaning, the samples were inserted into the radon monitor with their implanted side facing upwards towards the pin diode. Both samples lead to an increase in the activity of the ^{220}Rn decay chain products. Due to the lack of a ^{224}Ra source, the stored activity decreases with a half-life of 3.66 days[15]. The time evolution of the ^{212}Po activity is therefore not described by the ingrowth function $A^{ingrowth}_{^{212}\mathrm{Po}}(t)$ alone (Equation A.1). It needs to be convoluted with the exponential decay function, describing the decay of ^{224}Ra in the sample.

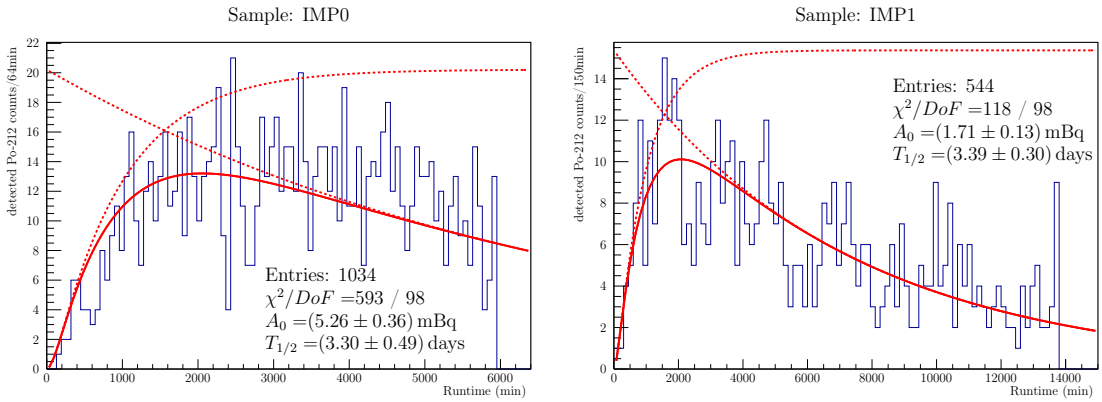

Figure 3.6: Time evolution of the detected activity found in the ^{212}Po peaks of the aluminum stripes (**left**) and the stainless steel plates (**right**) after implantation by recoil. The fit function as described in the text allows extraction of equilibrium activity A_0 and half-life $T_{1/2}$ which in both cases is in agreement with the literature value of the ^{224}Ra half-life of 3.66 days [15].

$$A_{212\mathrm{Po}}(t) = A_{212\mathrm{Po}}^{ingrowth}(t) \cdot e^{-\lambda_{224\mathrm{Ra}} t} \tag{3.3}$$

Figure 3.6 shows the time evolution of ^{212}Po activity after implantation for both samples. The above fit function reproduces the data reasonably well and allows to extract the ^{212}Po equilibrium activity A_0. For the case of the first measurement, data was taken shorter, which results in a less reliable fit showing a high χ^2/DoF value.

To get a limit on the activity caused by thoriated dust that sticks to the surface during preparation of the sample, a test with short implantation duration was done. For this test, the four aluminum stripes from sample IMP0 were re-used after their first implantation. The preparation procedure was reproduced as close as possible. However this time the implantation lasted only for 7 min[2]. An averaged activity of $(34.10 \pm 5.08)\,\mu$Bq was detected from this sample. Given that the background rate in ^{212}Po is expected to be $(20.97 \pm 4.81)\,\mu$Bq, no significant increase in the activity was detected.

Discussion and outlook The difference in the achieved activities of the two samples can be explained by their geometric coverage of the surface of the welding rods. Since in the case for IMP0, the 14.8 cm long aluminum foil stripes were wrapped around each 17.5 cm long welding rod separately, they cover 84.6% of the rods surface. The steel plates are lying on top of the welding rods as is depicted in Figure

[2]The amount of ^{224}Ra , implanted after this duration is expected to be $(4.08 \pm 0.29)\,\mu$Bq.

Table 3.3: Resulting activities from the samples implanted with recoiling ^{224}Ra from ^{228}Th decay.

Sample	$t_{implant}$	^{224}Ra yield	detected $A_0(^{212}\text{Po})$
IMP0	28 days	99.5 %	(5.26 ± 0.36) mBq
IMP1	21.79 days	98.4 %	(1.71 ± 0.13) mBq

3.5. This configuration is less efficient, since part of the solid angle is not available for the implantation, since it is blocked by a neighboring rod. Following this argument and given their length of 10 cm, they effectively cover only 28.6% of the available surface.

Implantation of radioactive isotopes by recoil of a preceding alpha decay, can be a method to produce samples to study radon mitigation. The shown results were so far considering the implantation of ^{224}Ra , which limits the sample to the study of ^{220}Rn emanation. Because of the short half-life of ^{224}Ra , the radon emanation rate is changing on a time scale of days. This makes it impractical to perform measurements using the same sample several times without re-implanting it.

The obtained results however may pave the way for another method to implant ^{226}Ra . From the surface of a ^{230}Th source, ^{226}Ra nuclei are released by alpha decay with an energy of 82.96 keV. The necessary activity $A_{230\text{Th}}$ of a source able to implant an activity $A_{226\text{Ra}}$ of ^{226}Ra within a given time $t_{implant}$, can be calculated by:

$$A_{230\text{Th}} = \frac{2 \cdot A_{226\text{Ra}}}{\lambda_{226\text{Ra}} t_{implant}}$$

Where $\lambda_{226\text{Ra}}$ is the decay constant of ^{226}Ra and the factor of 2 accounts for the loss of nuclei emitted not in direction of the sample. Production of a sample containing $A_{226\text{Ra}} = 1$ Bq within $t_{implant} = 30$ days would require a ^{230}Th source of 56.17 kBq. This translates to a ^{230}Th mass of 73.6 μg. However the effective thickness of such a source is limited to a few tens of nanometers by the short recoil range of the nuclei.

3.2 Coating techniques

The coating techniques that were investigated include two different PVD (**P**hysical **V**apor **D**eposition) processes as well as an electro-deposition procedure. In general PVD corresponds to the techniques in which the coating material is first transfered into the gas phase and then condensates onto the surface of the workpiece. Most of them require the use of an evacuated coating chamber. Electro-deposition produces a coating layer by chemical reduction of metal ions on the surface of the workpiece.

Metal ions are supplied by an electrolyte and the reaction is usually driven by an electric power supply.

3.2.1 Sputtering

One widely applied technique of PVD is sputtering. Sputtering describes the physical mechanism by which atoms from the surface of a solid target can be ejected by impacting ions. For this process, the workpiece is placed adjacent to the sputtering target inside a vacuum chamber. After evacuation the chamber is filled with a low pressure of argon gas of about 10^{-2} mbar [40]. A negative high voltage is applied to the sputtering target, whereas the workpiece is put on ground potential. This produces an electric field within the coating chamber. Free electrons, produced by interaction of ambient radiation with the gas, get accelerated in the electric field. Collision of these electrons with gas atoms, leads to further ionization and to formation of a stable glow discharge. The produced argon ions in turn get accelerated towards the sputtering target. By impacting the target, the gas ions transfer momentum on atoms from the target material, sufficient to release them from the target surface. Due to their remaining momentum, the ejected atoms traverse the coating chamber and deposit on the workpiece as a coating layer [40]. Figure 3.7 shows this process schematically.

DC magnetron sputtering: To increase the achieved deposition rate on the surface of the workpiece, the ionization rate needs to be increased. A higher rate of produced ions will lead to a higher sputtering rate. Increasing the argon pressure in the chamber would lead to more ionization, but would also decrease the mean free path of the sputtered atoms. This contradiction for long posed a physical limitation on the deposition rates achievable by sputtering[40].

Permanent magnets, that are installed underneath the sputtering target, can produce a magnetic field configuration that traps the electrons to an area close to the sputtering target[41]. By this their path through the gas is strongly increased, leading to a higher ionization yield without the need to increase the argon pressure[40]. Usually these magnets are embedded in a water cooled copper support to provide a high electric and thermal conductivity[40].

All of the samples that were coated with this technique were produced in cooperation with EC Europ Coating GmbH[3] in a DC magnetron sputtering chamber. Before placing the samples into the coating chamber, they were de-greased (in an ultrasonic bath containing iso-propanol). After evacuation and baking, argon is inserted into the coating chamber (to a pressure of 10^{-2} mbar). Prior to the coating process, the sample needs to be plasma etched in order to achieve a high adhesion on its surface. This is done by reversing the electrical field in the chamber which

[3] www.europcoating.com

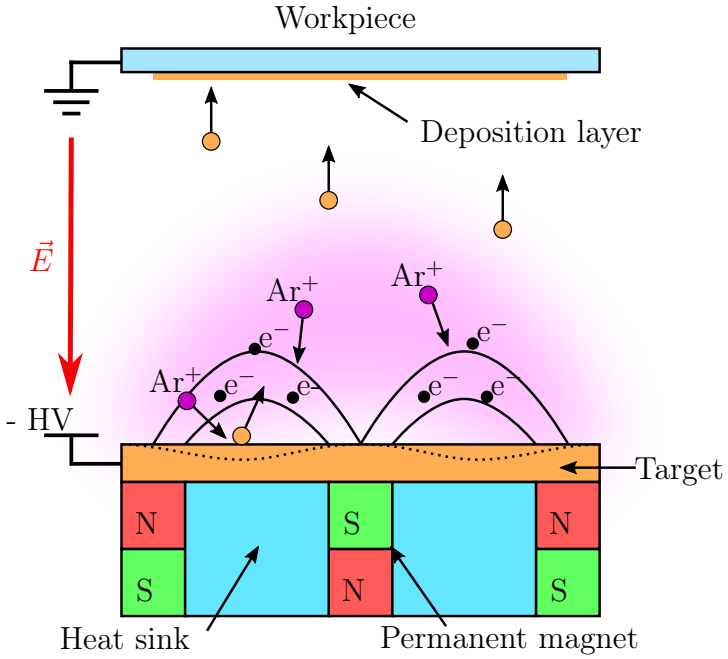

Figure 3.7: Setup used for DC magnetron sputtering. Argon is ionized by collision with electrons. The ions are accelerated by a high voltage and impact the sputtering target, ejecting atoms of the coating material, that then deposits on the surface of the workpiece. A magnetic field caused by permanent magnets confines the electron trajectories to increase the ionization rate.

leads to acceleration of the argon ions towards the work piece. The incident argon ions impact on the workpiece's surface and erode its top layer which usually consists of oxides. After reversing the applied voltages again, the coating process starts. Since sputtering works by the kinetic transport of the coating material, parts of the sample that are covered, don't receive any flux of coating material. Fixation of the samples in the chamber required the use of a clamp, shadowing parts of the surface. Therefore, two coating cycles per sample were required The sample was turned in between the two coatings.

Properties of the deposited layer Determination of the thickness of the coating layer was done using a reference sample, coated alongside with the workpiece. Afterwards, the reference samples surface is worn off by a rotating steel ball with a known diameter R. With an optical microscope the projected diameters r_a and r_b (see figure 3.8, right) can be measured. Under the assumption that the deposition rate on the reference sample is comparable with the deposition rate on the actual workpiece, the coating thickness d_{coat} can be estimated as follows[42]:

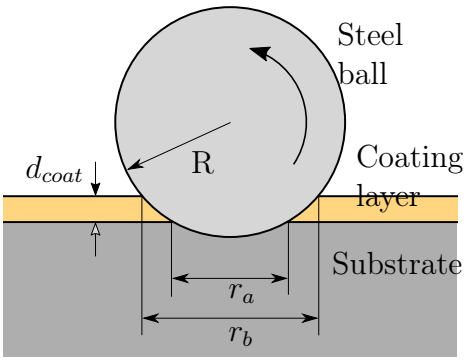

Figure 3.8: Technique for the estimation of the thickness of the coating layer using a reference sample.

$$d_{coat} = \sqrt{R^2 - \left(\frac{r_a}{2}\right)^2} - \sqrt{R^2 - \left(\frac{r_b}{2}\right)^2}$$

$$\Rightarrow \quad d_{coat} \approx \frac{r_b^2 - r_a^2}{8R} \qquad (\text{for } \mathrm{d_{coat}} \ll \mathrm{R}) \tag{3.4}$$

For the produced samples, this method suggested an increase in the coating thickness of about 400 nm per coating cycle. Which suggests, that the thickness of the coating range from 400 nm to 800 nm. The thickness at the areas that were covered by the fixation during one of the two coatings is expected to be 400 nm and the thickness in the middle is 800 nm.

It was reported [43] that the resulting microscopic structure of sputter coated surfaces depends on the temperature of the workpiece and the pressure of argon in the coating chamber. By an increase of the workpiece temperature during the coating process, a more dense surface might be achievable. The coatings in this work were done without active heating of the sample.

3.2.2 Plasma deposition

Another coating process was investigated, in which a high velocity plasma jet is employed in order to spray molten and evaporated metal powder onto the workpiece surface. Samples produced by this technique were obtained in collaboration with Dr. Laure Plasmatechnologie GmbH[4].

Setup and coating process: The workpiece is placed into a vacuum chamber opposite to a plasma gun as depicted in Figure 3.9. Inside the plasma gun, a process gas, argon or nitrogen, gets ionized by a high voltage and expands through a nozzle. At the outlet, the coating material gets injected into the stream in form of

[4]www.laure-plasma.de

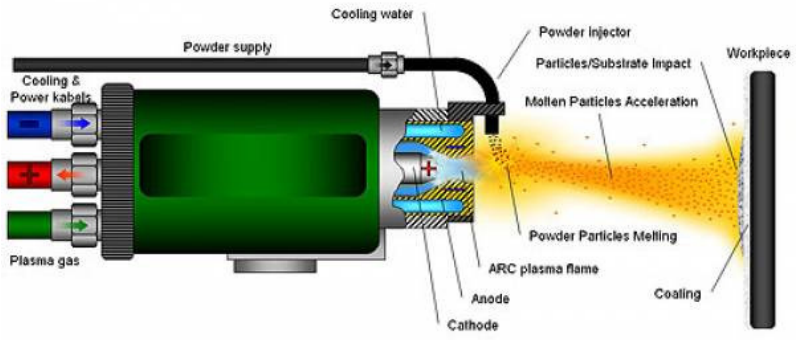

Figure 3.9: Setup for plasma coating. Coating material is sprayed as a fine powder into a stream of plasma produced by electrical discharge. The material melts and evaporates in the plasma and gets carried towards the workpiece, where it deposits as a coating layer. Figure taken from [45]

fine powder. Due to the high temperature of the plasma, the material melts and partially evaporates. Driven by the plasma stream, it impacts the workpiece surface and forms a coating layer [44].

All samples that were coated using this technique, were thoriated tungsten welding rods of 1 mm and 4.8 mm in diameter. The samples were coated by attaching them to a motor using one of the fixations depicted in Figure 3.10. They were then introduced into the plasma stream, while a rotary motor turned the sample, such that all sides could be covered. In order to also coat the part of the sample that was covered by the holder, the coating process was repeated, with the sample attached on the other side.

Estimation of layer thickness: The thickness of the coating layer was inferred by the weight increase m_{coat} of the sample after the coating. If the coated surface A of the workpiece is known, it is possible to estimate the thickness d of the coating layer.

$$d = \frac{m_{coat}}{\rho \cdot A} \tag{3.5}$$

Where ρ is the density of the coating layer, for which an assumption must be made. Samples using this technique were coated with copper. Assuming that the density of the coating layer is comparable to solid copper, the coating thicknesses achieved by this method are in the range of 2 μm to 3 μm.

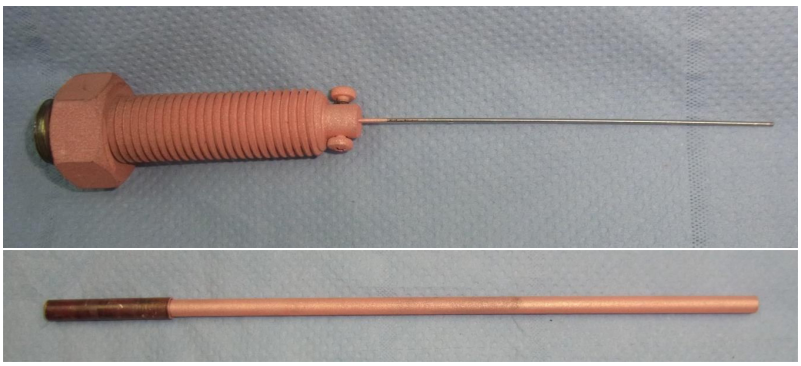

Figure 3.10: Different versions of the fixation for the coating samples. **Top:** Fixation for 1 mm thick electrodes. **Bottom:** First version of the holder for 4.8 mm thick electrodes.

3.2.3 Electrodeposition

Electrodeposition forms a solid metal layer on the workpiece by electrochemical reduction of metal ions from a liquid solution. The process is driven by a power supply, connected to two electrodes, that are submerged in the coating electrolyte.

Setup of the coating cell All coatings of this type have been performed at MPIK, using the setup shown in Figure 3.11. The setup consists of a beaker in which solid copper-sulfate ($CuSO_4 + 5H_2O$) was dissolved in de-ionized water (Milipore 18.5 MΩ) to achieve a concentration of 0.05 mol/l . In addition, sulfuric acid (H_2SO_4) was added with a concentration of 1 mol/l. This solution is based on the one described in [46]. A heater plate with a magnetic steerer was used to maintain the solution at a temperature of approximately 40 °C. It was found that the heat and agitation of the electrolyte, strongly improved the outcome of the coating. For the positive electrode, a platinum mesh was used and the negative pole was connected to the workpiece. The current flowing through the coating cell was monitored and recorded.

Coating procedure: Before coating, each workpiece was cleaned in order to free the surface from grease. By this it should be ensured that the coating liquid is in uniform contact with the surface. The samples were cleaned by using lab tissues and acetone, iso-propanol and deionized water [46].

Due to limited height of the beaker and the need for the electrical connection, part of the workpiece was ranging out of the liquid level. Therefore each sample was coated twice, and the sample was turned in between the two processes in order to cover its entire length.

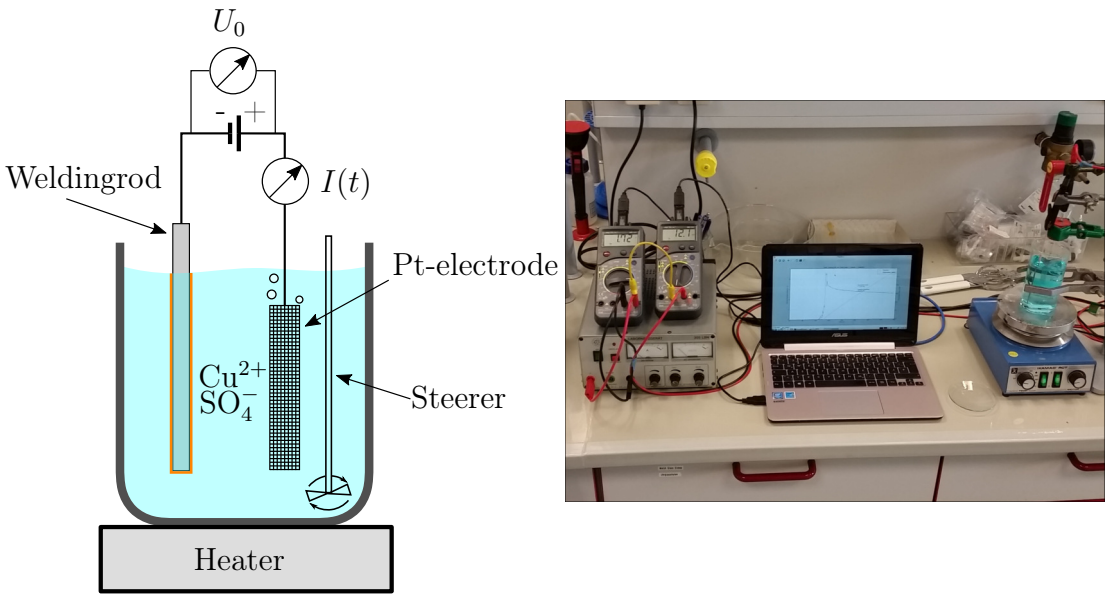

Figure 3.11: **Left:** Schematic of the coating cell used for electrodeposition of copper on a thoriated tungsten rods. **Right:** Picture of the setup in the lab.

A non uniform coverage of the surface of the samples during the coating process was noticed. Figure 3.12 shows microscopic photographs of a cross section through a coating, prepared on a tungsten rod with a diameter of 4 mm. The pictures show that the surface structure varies along the circumference of the workpiece. This in-homogeneity might have been caused by turbulent flow of the electrolyte around the circumference of the workpiece. In Figure 3.12 the electrolyte on-stream side was located around the lower left corner of the sample. To increase the uniformity of the coating, samples were rotated twice during the coating process.

Coatings of tungsten surfaces were prepared using a constant voltage of 2.08 V. The coating on stainless steel surfaces required an increased voltage of 2.58 V to form an adhesive copper layer. After 45 sec the steel surface was covered with copper, and the voltage was reduced to 2.15 V. Copper layers that were deposited at this lower voltage had an optically similar appearance to the layers deposited on tungsten surfaces.

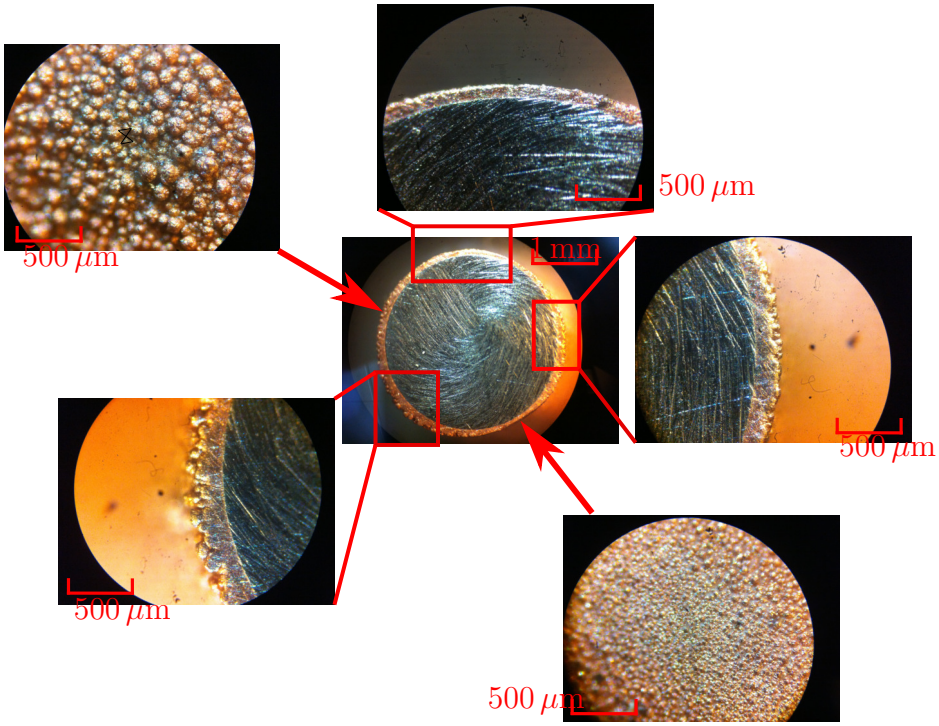

Figure 3.12: Microscopic investigation of a cross section of a 4 mm thick tungsten wire, copper coated by electrodeposition. Surface thickness was estimated to be 133 µm by relative weight increase. Different structure of the surface along the circumference might be caused by turbulent flow of the electrolyte.

Determination of the thickness The reduction reaction taking place on the workpiece surface, is given as

$$\mathrm{Cu^{2+}(aq) + 2e^- \rightarrow Cu(s).} \tag{3.6}$$

The number of copper ions N_{Cu} that were reduced during the coating is directly related to the total charge Q_{tot}, that was passing through the electric circuit

$$N_{Cu} = \frac{Q_{tot}}{2e} = \frac{1}{2e} \int_{t_s}^{t_e} I(t)dt. \tag{3.7}$$

The total charge can be determined by integrating the current over time from t_s (start) to t_e (end). Here, e is the elementary charge and the factor of two is necessary since each cooper ion requires two electrons to be reduced to neutral copper.

The mass of copper m_{Cu}, deposited on the workpiece can be calculated using the molar mass M_{Cu} of copper and Avogadro's constant N_A

$$m_{Cu} = \frac{N_{Cu}}{N_A} \cdot M_{Cu}. \tag{3.8}$$

The mass increase of each sample was additionally measured using a scale. In most of the cases, both methods were in good agreement. Knowledge of the surface A of the coated workpiece and making an assumption on the density of the coating layer, allows to estimate its thickness d by formula 3.5. A direct measurement of the thickness a coating layer was possible for the case of the sample shown in Figure 3.12. Using the cross-hair, embodied in the ocular of the microscope, the thickness was estimated at several positions along the samples circumference. Due to the described in-homogeneity, results vary between 100 μm to 200 μm. The estimated coating thickness using the increase of the mass and using the density of solid copper suggested a thickness of 133 μm. Which is in agreement with the observation. Besides this coating specially prepared for optical investigation, the samples coated by electrodeposition were produced with thicknesses between 2 μm and 10 μm.

Normalizing the measured current by the coated surface, gives the surface current density j. It is directly proportional to the deposition rate and strongly related to the resulting micro structure of the coating layer [47]. Therefore it might have an influence on the radon mitigating properties of the coating layer. In order to keep the results from different samples comparable, the coatings were prepared with a surface current density between 6 mA/cm^2 and 8 mA/cm^2.

3.3 Characterization of coating layers

Several methods were used to determine the quality and the properties of the deposited layers. Mechanical and microscopic tests were done during sample preparation in order to find a reliable coating procedure for the production of an adherent

deposition. Tests addressing their radon mitigating properties where done afterwards to evaluate the efficiency of the coating.

3.3.1 Microscopic and mechanical tests

Electron microscope: Using a **S**canning **E**lectron **M**icroscope (SEM), it is possible to obtain images from the surface topography of the specimen with a good resolution. Additionally, the instrument available at Dr. Laure Plasmatechnology GmbH in Stuttgart employs a **B**ack **S**catter **E**lectron (BSE) detector, with which images showing a high material contrast can be produced.

The image is generated by scanning the surface with a beam of electrons ($1 - 50\,\mathrm{keV}$).

Secondary **E**lectrons (SE) are produced by interaction of the primary electron beam within the material of the sample. Due to their typically low energy of less than 50 eV, they can escape the sample only from shallow depths of a few nanometers. The amount strength of the detected SE signal, depends on the orientation of the surface element, that is irradiated and therefore contains information on the topography of the surface of the sample.

BSE can emerge from the elastic scattering of the primary electrons in the Coulomb field of the nuclei of the material. The scattering probability is a function of the atomic charge and scales with Z^2. It therefore is possible to achieve a high material contrast with regard to the atomic number when recording the BSE signal [48]. The investigation of thoriated tungsten ($Z_W = 74$) rods, covered with copper ($Z_{Cu} = 29$) or titanium ($Z_{Ti} = 22$), is an ideal case to employ this detection method. Due to the high difference in atomic number of the substrate and the coating material, the BSE signal is expected to be very sensitive to defects and non covered parts of the surface.

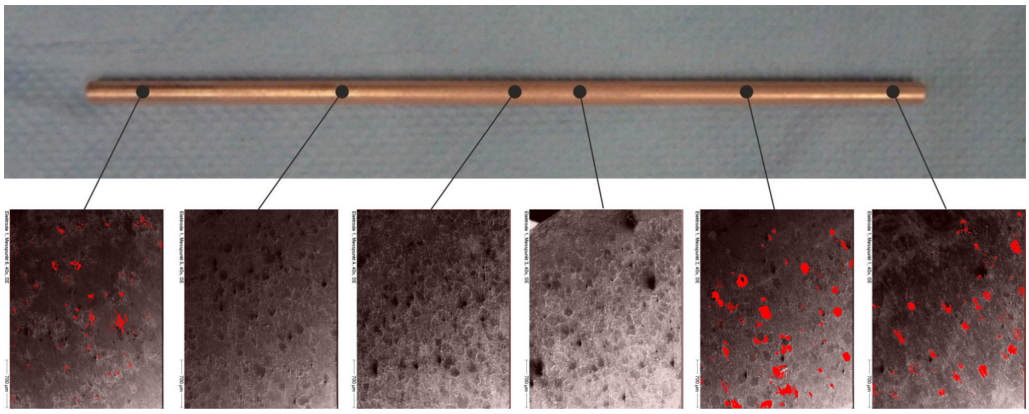

Figure 3.13: Investigation of a 4.8 mm tungsten rod, after two applications of copper coating by plasma deposition. Grayscale image corresponds to the secondary electron signal. The overlayed red images corresponds to the signal from the back scattered electrons, revealing defects in the coating layer. Images provided by Dr. Laure Plasmatechnology.

Figure 3.13 shows sample images of an intermediate result in the coating of a 4.8 mm thick thoriated tungsten welding rod. The grayscale images correspond to the secondary electron signal, whereas the red overlay shows the strength of the BSE signal for the corresponding point on the surface. It can be seen that in the present case, defects in the coating are still visible towards the ends of the sample, where it was attached to the holder during the coating process.

Scotch tape test: This is a widely applied test to determine the adhesion properties of a deposited coating layer [49]. A stripe of adhesive tape is placed onto the coated surface. By applying pressure, the adherence of the tape to the coating is ensured. In addition, mechanical stress on the surface was exerted by bending the sample. The tape is then ripped off from the surface and the adhesive side of the tape is investigated. Complete or partial removal of the coating layer is a sign of poor adhesion. Only an undamaged surface with no coating material sticking to the adhesive tape suggests a reasonable adherence of the coating layer.

Thermal stress test To be usable in cryogenic environments like liquid xenon detectors, the coating layers must maintain their adhesion and radon mitigating properties under cryogenic conditions. Due to the difference in the thermal expansion of different material, the inter layer between the substrate and the coating material can be exposed to increased stress caused by changes in temperature. This can lead to damages and loss of adhesion of the coating layer.

Table 3.4: Linear thermal expansion coefficient α for the different substrate and coatings materials in this work [50].

Material	expansion coefficient (ppm/K)
Tungsten	4.6
Stainless steel	16.0
Copper	16.5
Titanium	8.41

Table 3.4 shows the linear thermal expansion coefficients α for metals, that were relevant in this study. The change of the length L of an object by an amount ΔL due to a change in temperature of ΔT, can be approximated by the linear relation [51]

$$\frac{\Delta L}{L} = \alpha \Delta T.$$

In order to judge the thermal stability of a coating layer, it was submerged into a bath of liquid nitrogen several times. Intermediate measurements of the radon

reduction provided by the coating, as well as weight measurements, were done to detect a possible change of the coating properties due to the thermal stress. This test can be regarded to be more demanding on the thermal stability of the coating layer due to the following reasons. The temperature to which the sample is exposed in this test, is roughly $-196\,^{\circ}\mathrm{C}$, which is significantly lower than typical temperatures present in liquid xenon detectors ($-110\,^{\circ}\mathrm{C}$). Furthermore, the sample which initially is at room temperature, gets directly submerged in the liquid nitrogen. It can be expected, that the decrease in temperature for a liquid xenon detector is gradual over a longer time span.

3.3.2 Determination of the radon mitigating properties

The main focus of this work is the radon reduction by applied coating layers. Therefore the quality of the coatings will be judged by their radon mitigating properties.

^{224}Ra mitigation Besides ^{220}Rn, the uncoated thoriated tungsten welding rods release ^{224}Ra [30]. Its contribution to the spectrum as acquired using the radon monitor (see Section 2.2.2) can be seen for example in Figure 2.5. Since radium is non gaseous, its diffusion in the welding rod should be highly suppressed. Therefore its release mechanism is understood to be purely due to the recoil of the previous alpha decay of ^{228}Th . By application of a coating layer with a thickness sufficient to stop the recoil of ^{224}Ra and covering the complete surface of the welding rod, the ^{224}Ra contribution to the spectrum can be efficiently eliminated. As a consequence the detection of ^{224}Ra in the spectrum acquired using a coated sample can be a hint to incomplete coverage of the samples surface by the coating layer.

Since the decay energy of ^{224}Ra is close to that of ^{212}Bi , their peaks in the energy spectrum overlap. To reduce the bias introduced by the tail of the ^{212}Bi peak on the activity of ^{224}Ra , the fit function of the spectrum as described in Section 2.2.2 was used. With this the ^{224}Ra activity can be extracted, or an upper limit on it can be given.

Radon reduction factor The radon reduction provided by a coating layer was determined by comparison of the radon emanation rate before and after application of the coating. If A_b is the radon activity before coating while A_a is the respective quantity after coating, the radon reduction factor R is given by:

$$R = \frac{A_b}{A_a}. \tag{3.9}$$

The error on the reduction factor was determined by error propagation (Equation C.3). Most of the measurements were repeated several times to get a more reliable result on the emanation rate. In these cases, the activity was then calculated as the weighted mean over the single measurements (see Appendix C.1).

Temperature dependence of the radon emanation As described in 2.1.1, it is expected that diffusion driven radon emanation would show a significant temperature dependence, whereas recoil dominated emanation would not. The setup shown in Figure 3.14 was designed, to study the effect of temperature on the emanation process.

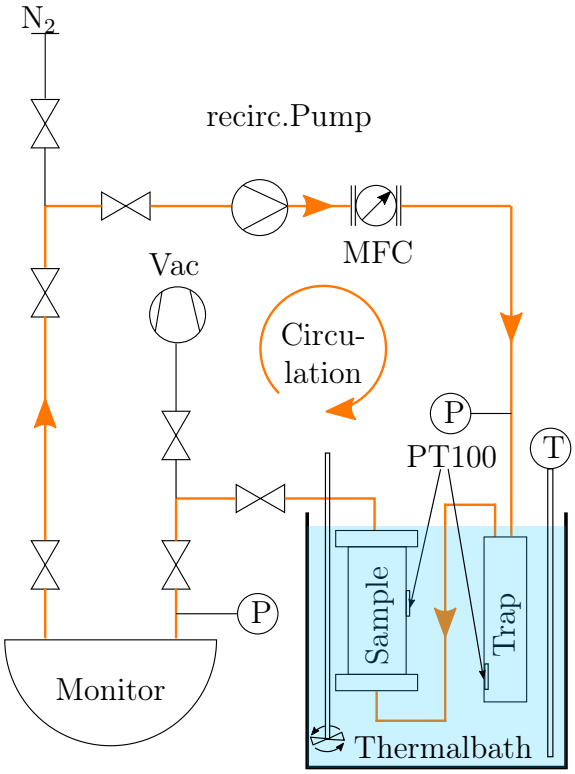

Figure 3.14: Scheme of the setup, that was used to determine the temperature dependence of the radon emanation rate. The sample is stored in an emanation vessel, that is submerged in a thermal bath. Radon emanated from the sample is introduced to the radon monitor by a circulation flow. The flow is monitored using a MFC. A cold trap was used to ensure, that the gas temperature is equal to the temperature of the thermal bath, which is monitored by PT100 temperature sensors.

The radon monitor was connected to a gas recirculation loop. Gas flow was driven by a piston pump and monitored by an MKS mass flow controller (MFC). A double walled Dewar filled either with water or a mixture of water and glycol based anti-freeze agent was used as a thermal bath. The gas flow was pre-cooled using an active charcoal trap, that was submerged in the thermal bath together with the emanation vessel containing the sample. A PT100 temperature sensor inside the trap was used to measure the temperature. For measurements below room temperature, a diving chiller was used. The minimum achievable temperature about $-30\,°C$. Measurements above room temperature were performed using a circulation heater,

with which temperatures as high as +60 °C were obtained.

The parameters of the setup (pressure, circulation flow and temperature) were monitored during each measurement. An example of the stability of these systematic parameters is shown in Figure 3.15 for an emanation temperature of −30 °C.

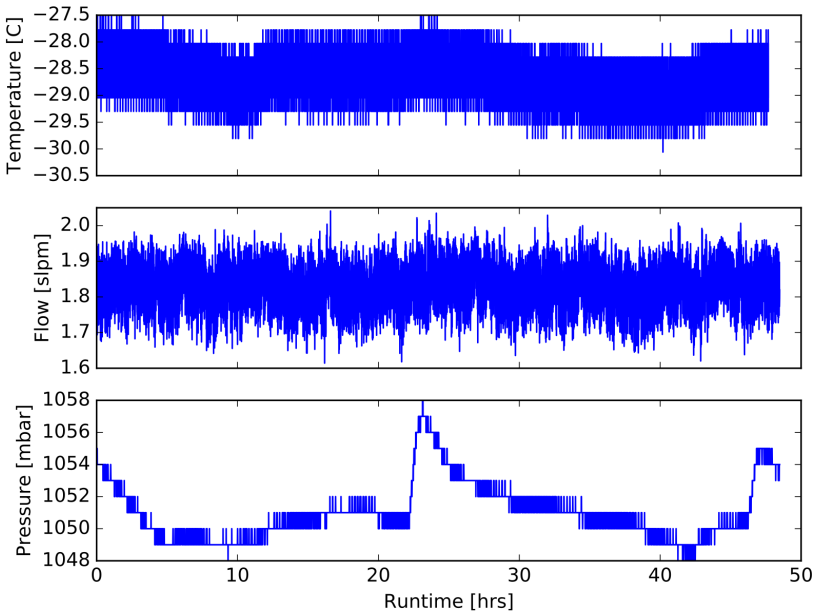

Figure 3.15: Systematic parameters of the thermal emanation setup for a measurement taken at about −30 °C. The system is stable beisdes small irregularities in the pressure that were caused by the sun shining on the setup.

The gas needs on average a time τ to reach from the emanation vessel to the detector. During this time, some of the emanated radon activity A_0 can already decay, such that only an activity A_{mon} enters the radon monitor.

$$A_{mon} = A_0 \cdot e^{-\lambda\tau} \tag{3.10}$$

where λ is the decay constant of the considered radon isotope. An estimate of the retention time can be given by the ratio of the volume of the emanation vessel V_v and the volumetric flow Q_v inside it.

$$\tau = \frac{V_v}{Q_v} \tag{3.11}$$

The MFC outputs the flow in terms of the corresponding volumetric flow Q_s at standard temperature ($T_s = 0\,°\mathrm{C}$) and pressure ($P_s = 1013\,\mathrm{mbar}$). To account for

the different temperature in the emanation vessel, the flow needs to be re scaled as follows [52]:

$$Q_v = Q_s \cdot \frac{P_s}{T_s} \cdot \frac{T_v}{P_v}. \tag{3.12}$$

Where T_v and P_v are the temperature and pressure inside the emanation vessel. By combining the equations above, a correction factor $R(T_v)$ can be defined as:

$$R(T_v) = \frac{1}{R(0)} \cdot e^{\frac{\lambda}{Q_v}}, \tag{3.13}$$

with which each measurement needs to be scaled. To remove the unknown emanation rate A_0, the correction factor was normalized using $R(0)$ such that it equals 1 for a temperature of 0 °C. The systematic error σ_R was determined by error propagation using the standard deviations of the systematic parameters. It can be found in Appendix C.

This setup was used to determine the temperature dependence of the ^{220}Rn emanation through a sputtered titanium layer. The results on this are reported in section 3.5.

3.4 Results and discussion

This section reports the results on the radon mitigating properties using the coating techniques described in 3.2 and the available information on the characterization of the coating layers using the methods shown in 3.3.

3.4.1 Activities of the samples before coating

From the samples described in Section 3.1, mainly the thoriated welding rods were used. These samples are abbreviated with "WTh-*". The sample that was produced using implantation of ^{224}Ra by recoil (IMP2) was also part of this study. Table 3.5 shows the activities of all used samples before the application of a coating layer.

Since no major difference between the activities of welding rods from different batches were found during this study, the previous table contains values determined using the global average over all samples. The deviation in the mean activity of different batches was assumed to be small and will not be further considered.

Table 3.5: Radon emanation of all used samples before application of coatings. ^{222}Rn activities as determined with miniaturized proportional counters. The ^{212}Po activitiy was measured with the radon monitor. d is the diameter of the rod and N the number of rods in the sample. N_{meas} indicates the number of individual measurements used to determine the activity.

Sample	d (mm)	N	$A(^{222}\text{Rn})$ (μBq)	N_{meas}	$A(^{212}\text{Po})$ (mBq)	N_{meas}
WTh1-1	1	5	229 ± 19	5	35.35 ± 0.25	2
WTh1-2	1	5	192 ± 18	5	33.95 ± 0.25	2
WTh2	1	6	-	-	44.47 ± 0.29[c]	3
WTh2-1	1	3	-	-	22.24 ± 0.15[a,c]	-
WTh3	1	6	-	-	39.75 ± 0.30[c]	2
WTh3-1	1	3	128 ± 6[b]	-	20.80 ± 0.22[c]	2
WTh4	4.8	6	-	-	78.52 ± 0.54	1
WTh4-2	4.8	1	-	-	11.71 ± 0.27	1
WTh4-3	4.8	1	-	-	12.98 ± 0.28	1
WTh5	4.8	10	663 ± 37	3	-	-
WTh5-1	4.8	7	453 ± 30	3	91.12 ± 0.16[a]	-
WTh5-2	4.8	3	-	-	39.80 ± 0.38	4
IMP2	1	2	-	-	1.71 ± 0.13	2

[a] Value determined using average from this batch.
[b] Value determined using global average over all batches.
[c] Measurement already reported in [30].

3.4.2 Activities of the samples after coating

Magnetron sputtered titanium layers Three different coating samples alongside with several mechanical sample were produced with the technique described in Section 3.2.1. The samples used for coating were in all cases thoriated welding rods with a diameter of 1 mm.

The first batch (WTh3-1) and the second batch (WTh-2) were coated in the Europcoating GmbH facility in Dresden. For the third batch (WTh1-1) another coating chamber in the Europcoating GmbH facility in Hohenlockstedt was used. Several mechanical samples were used to obtain an adherent coating layer as evaluated using the Scotch-tape test. Table 3.6 shows the activities obtained for these samples after coating.

Plasma deposition Two samples were successfully coated using this technique. The first batch (WTh2) consisted of six 1 mm thick WTh welding rods. During the coating process, three of the six rods were completely coated (WTh2-1), while

Table 3.6: Radon emanation of three samples coated with titanium by magnetron sputtering. N_{meas} indicates the number of individual measurements used to determine the activity.

Sample	d (mm)	N_{rods}	$A(^{222}\text{Rn})$ (μBq)	N_{meas}	$A(^{212}\text{Po})$ (mBq)	N_{meas}
WTh1-1	1	5	-	-	30.08 ± 0.05	3
WTh1-2	1	5	153 ± 21	3	22.81 ± 0.11	3
WTh3-1	1	3	61 ± 15	3	4.61 ± 0.05[a]	5

[a] Contains measurements that were already reported in [30].

the other three were partially coated. The second batch (WTh5-2) consists of three 4.8 mm thick WTh welding rods. So far one of these rods was successfully coated. The deposited masses and resulting surface thicknesses of these samples are summa-

Table 3.7: Radon emanation of two samples coated plasma deposition. N_{meas} indicates the number of individual measurements used to determine the activity.

Sample	d (mm)	N	$A(^{212}\text{Po})$ (mBq)	N_{meas}	Coating thickness
WTh2-1	1	3	9.81 ± 0.08[a]	6	$(1.48 \pm 0.07)\,\mu$m
WTh5-2	4.8	1	0.60 ± 0.05	1	$(3.15 \pm 0.16)\,\mu$m

[a] Contains measurements that were already reported in [30].

rized in Table 3.7. The error on the mass was estimated to be of the order of 5% and used to determine the error on the thickness of the coating layers. The activities of these two samples after coating is summarized in Table 3.7

Electrodeposition Samples using this technique were prepared according to the procedures described in 3.2.3. Three samples of 4.8 mm thick thoriated welding rods and one sample of ^{224}Ra implanted stainless steel plates were coated with different thicknesses of copper. Plots showing, the time development of the surface current density during the single coating processes are given in Appendix B.

The deposited masses are given in Table 3.8 and the detected activities after coating are summarized in Table 3.9.

3.4.3 Reduction factors due to coating

The reduction in the ^{222}Rn and ^{220}Rn emanation rate that was achieved for the single samples by application of a coating are shown in Table 3.10. They will be discussed in the next section.

Table 3.8: Average of the deposited mass by electrodeposition. The layer thickness was infered using Formula 3.5. Errors are assumed to be of the order of

Sample	Mass increase	Coating thickness
WTh4-2	(244.5 ± 1.4) mg	(9.66 ± 0.57) μm
WTh4-3	(125.6 ± 0.6) mg	(5.05 ± 0.03) μm
WTh5-1	(129.7 ± 1.0) mg	(5.00 ± 0.04) μm
IMP2	(101.1 ± 14.6) mg	(2.04 ± 0.15) μm

Table 3.9: Radon emanation of the four samples coated by electrodeposition. N_{meas} indicates the number of individual measurements used to determine the activity.

Sample	d (mm)	N_{rods}	$A(^{222}\text{Rn})$ (μBq)	N_{meas}	$A(^{212}\text{Po})$ (mBq)	N_{meas}
WTh4-2	4.8	1	-	-	0.11 ± 0.01	1
WTh4-3	4.8	1	-	-	0.27 ± 0.02	1
WTh5-1	4.8	7	61 ± 15	4	0.71 ± 0.02	2
IMP2	1	2	-	-	0.14 ± 0.04	2

3.5 Interpretation and Outlook

The first result for DC magnetron sputtering (WTh3-1) showed a promising reduction factor of 4.5. The samples that were coated afterwards using this technique could unfortunately not show a significant reduction factor. This case was investigated with the use of the SEM/BSE technique. Microscopic images were acquired for one rod of each sample which was inspected on four different spots along its axis. The result of this assay is shown in Figure 3.16.

From the images, it can be seen that the coating does not show significant defects since these would be visible as red areas, where the BSE signal would be enhanced by the presence of tungsten. The structure of the coating layers looks comparable for both electrodes. However, the left sample shows irregular features on some parts of its surface that could not yet be clearly identified. Three out of the five rods of sample WTh1-2 were inspected individually and showed no increased or decreased activity. This also excludes the possibility, that the coating of some of the rods was less efficient.

It was found that most of the samples that were coated with copper either by electrodeposition or by plasma deposition follow a linear relation between the ^{220}Rn reduction factor and the thickness of the coating layer (see Figure 3.17). This result has already been observed by [53, 54], where the diffusion of ^{222}Rn through polymer membranes and other radon proof material is investigated. Sample WTh5-1 seems to be an exception from this relation. One possible reason might be that it consists

Table 3.10: Radon reduction factors of all samples

Sample	Technique	$R(^{222}\text{Rn})$	$R(^{212}\text{Po})$
WTh1-1	Sputtering	-	1.18 ± 0.01
WTh1-2	Sputtering	1.26 ± 0.21	1.49 ± 0.01
WTh3-1	Sputtering	2.18 ± 1.66	4.51 ± 0.07[a]
WTh2-1	Plasma		2.27 ± 0.02[a]
WTh5-2	Plasma		22.0 ± 1.8
WTh4-2	Electro		107 ± 14
WTh4-3	Electro		47.4 ± 4.3
WTh5-1	Electro	7.9 ± 2.6	129 ± 3
IMP1	Electro		12.2 ± 3.6

[a] Result was already reported in [30].

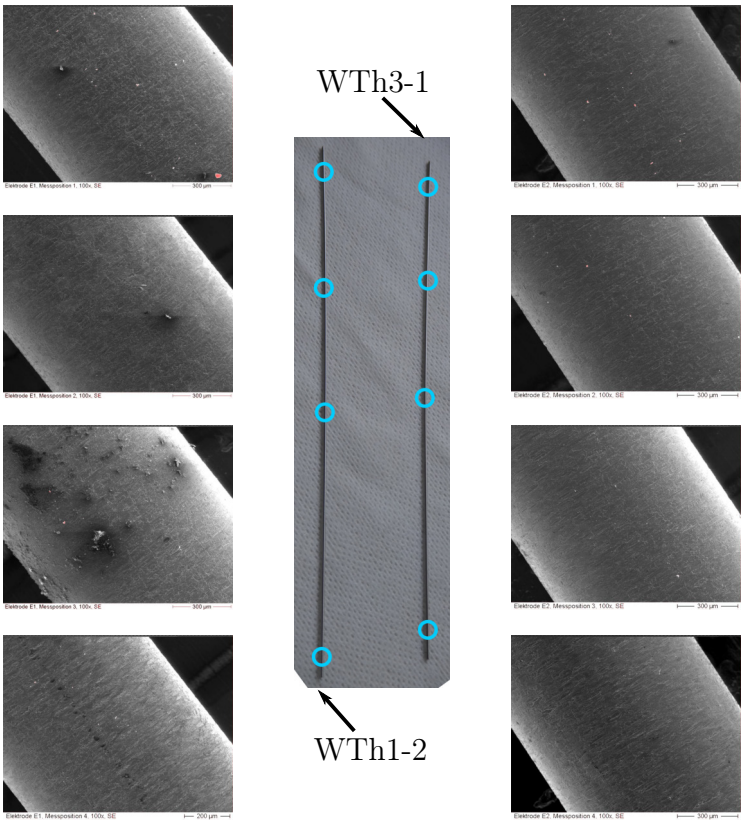

Figure 3.16: Comparison of the magnetron sputtered surfaces from two different batches. The SEM image shows the topology of the surface (gray scale), while the signal of the BSE detector (red) can highlight holes in the coating layer.

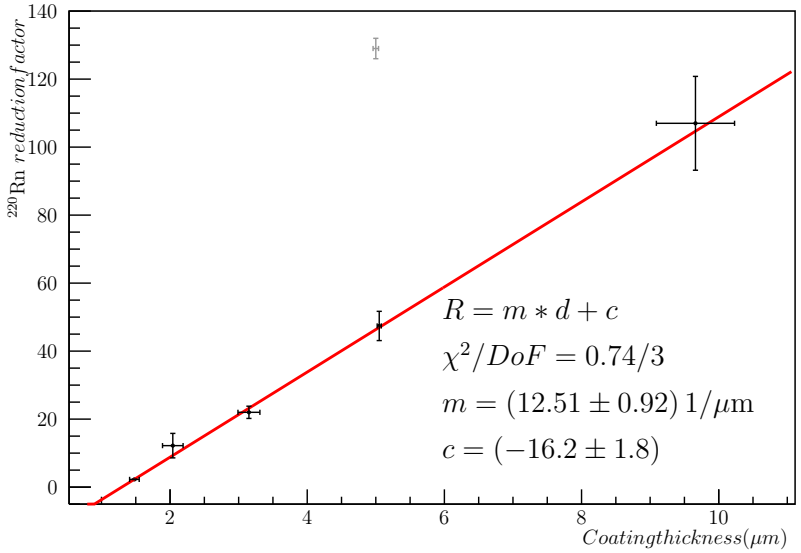

Figure 3.17: Plot of the reduction factor as a function of the coating thickness. A linear relation between the ^{220}Rn reduction factor and the coating thickness was found which most of the copper coated samples follow. The gray sample (WTh5-1) was excluded from the linear fit.

of seven coated welding rods, which are measured in the radon monitor simultaneously. Since they occupy a large fraction of the detection volume, the electric field responsible for collection of the radon daughters might be altered, leading to a change in the detection efficiency. And will be further investigated.

Another indication that the remaining emanation through a coating layer is diffusion driven results from the temperature dependence of the emanation. Using the setup described in Section 3.3.2, it was possible to study how the amount of ^{220}Rn emanated from the sputter coated sample WTh3-1 changes at different temperatures. Figure 3.18 shows the resulting activities in a temperature range from $-30\,^{\circ}$C to $+50\,^{\circ}$C. A clear temperature dependence is visible. A linear fit function was chosen. In [55, 56], a similar linear dependence was found for the temperature dependence of ^{222}Rn emanation from minerals. By linear extrapolation of this function, the temperature at which the emanation would be equal to zero can be determined to be $(-64.2 \pm 4.2)\,^{\circ}$C[5].

A first investigation of the thermal stability was done using the liquid nitrogen procedure as in Section 3.3.1. For the test, a sample produced by electrodeposition with a layer thickness of about $10\,\mu$m was chosen. Figure 3.19 shows the resulting

[5]Coincidentally this is in between the freezing point $71\,^{\circ}$C and the boiling point $61.8\,^{\circ}$C of ^{222}Rn [57].

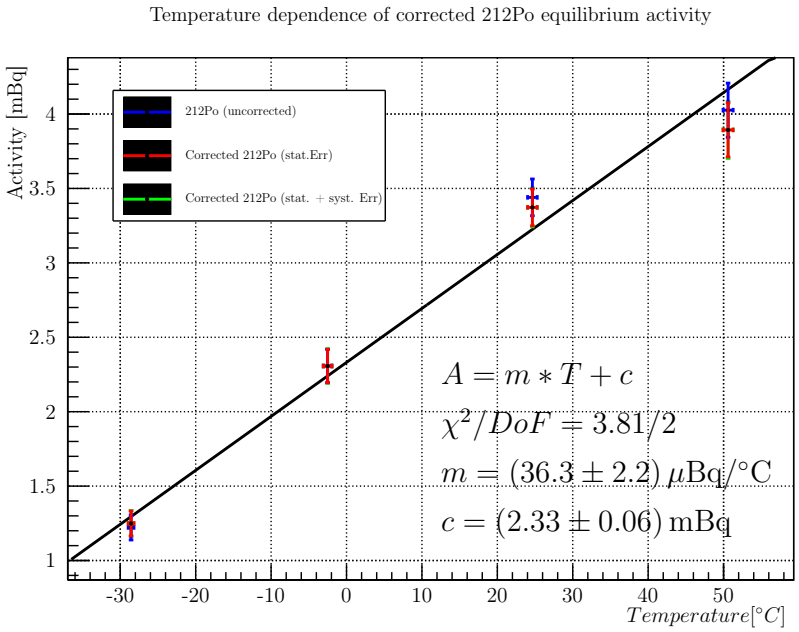

Figure 3.18: Result of the temperature dependence of the ^{220}Rn emanation through a sputtered titanium coating. For information on the applied correction, see Equation 3.13

^{220}Rn emanation rate before the test, compared with the emanation after two and ten fold submersion in the liquid nitrogen bath. A slight decrease in the radon mitigating properties might be hinted by the measurements, however more data needs to be acquired.

The indications for a diffusion driven emanation through the coating layer could be promising for their application in liquid xenon detectors. However, it must be proven that the coating layer is stable in cryogenic environments and that it maintains its radon mitigating properties. Furthermore it needs to be investigated, wheather either the coating material or any residues from the coating process can have an impact on the detector performance. The HeXe system which will be described in the next chapter will be employed to test the applicability of the coating layers under operating conditions.

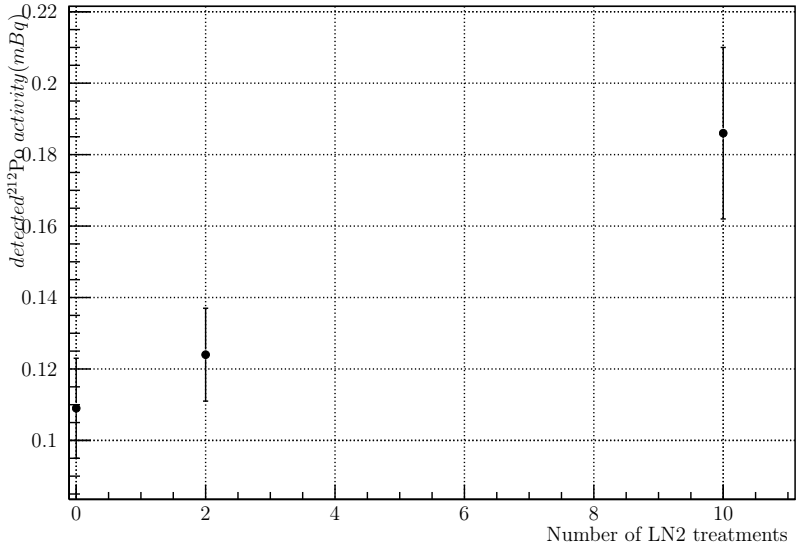

Figure 3.19: Behaviour of the ^{212}Po equilibrium activity after exposing the sample to thermal stress by submersion in liquid nitrogen for several iterations.

4 Purity in liquid xenon detectors and the HeXe setup

Liquid noble gas detectors are among the leading technologies for rare event searches such as direct dark matter detection. One example is the XENON1T TPC (**T**ime **P**rojection **C**hamber), described in section 1.2. A high purity of the liquid xenon is crucial for the functioning of the detector [58]. The HeXe (**He**idelberg **Xe**non) system at the MPIK[1] is currently being prepared to host a dual-phase liquid xenon TPC. One purpose of this detector will be to study how impurities that could get dissolved from material surfaces impact the performance of the detector. It is also planned to employ this detector to test the stability and influence of surface coatings in real operating conditions using liquid xenon.

4.1 Influence of impurities in dual-phase time projection chambers

As described in section 1.2, a dual phase TPC relies on the simultaneous detection of a light signal S1 and a charge induced signal S2. Impurities, that are dissolved in the liquid xenon, can lead to an attenuation of these two signals. While the electrons drift from the interaction site to the liquid-gas interface, they can get attached by polar molecules contaminating the xenon. These so-called "electronegative impurities" are for instance O_2, H_2O and N_2O [59]. The number of electrons $N(t)$, that are remaining for creation of a S2 signal, decreases exponentially with the drift time t due to the loss of electrons by attachment to impurities [60].

$$N(t) = N_0 \exp\left(-\frac{t}{\tau}\right) \tag{4.1}$$

where N_0 is the number of electrons produced by the interaction and τ is the electron-lifetime. The electron lifetime is inversely proportional to the concentration of electronegative impurities present in the liquid xenon. Alternatively, it can be expressed as the attenuation length of the electrons λ_{att}, which depends on the electron mobility μ_e in liquid xenon and on the electric field strength E [59]

$$\lambda_{att} = \mu_e E \tau. \tag{4.2}$$

[1] Max-Planck-Institut für Kernpysik Heidelberg

To achieve an attenuation length of at least 1 m, an oxygen concentration below 1 ppb is required.

The scintillation light of xenon, has a mean wavelength of 177.6 nm [61]. It receives strong absorption by residual water and oxygen, that is dissolved in the liquid xenon. An attenuation length of the scintillation light of more than 1 m can be reached when the concentration of residual water reaches a level below 100 ppb [59]. It is therefore expected, that the effects of impurities on the electron lifetime are more stringent than their impact on the scintillation light. Techniques for radon mitigation using coating or chemical cleaning agents (not discussed in this work), could potentially decrease the xenon purity. Especially if traces of chemicals remain on their surface and get dissolved in the xenon.

4.2 Detector setup

The HeXe TPC will be housed in a cryostat for the operation with liquid xenon. Liquification of gaseous xenon is using a copper cold head, coupled to a helium compressor. Xenon recirculation and purification is provided by a dedicated gas system, using a hot metal getter. System parameters such as pressure, recirculation flow and temperature are monitored using a slow control system. The signals detected by the two PMTs (**P**hoto**m**ultiplier **T**ubes) are digitized and recorded by a DAQ system. Details on the HeXe setup can be found in [16] and [62].

4.2.1 Gas system

The gas system is dedicated to maintain the purity of the xenon, serve as an interface for radioactive sources and material samples, as well as to the recuperation of the xenon into a storage cylinder. Figure 4.1 shows a schematic overview of the gas system.

During detector operation xenon is constantly removed from the cryostat, purified and reintroduced into the detector. This recirculation flow is driven by a KNF N 143 double diaphragm pump. It can provide a gas flow of 30 slpm at a maximum operating pressure of 3.0 bar [63]. For adjustment and monitoring of the flow, a MKS 1179A mass flow controller is installed in the purification loop. Purification of the xenon in the system is achieved using a SAES PS4 MonoTorr getter [64]. During operation, the flow is guided through the hot getter, with a nominal flow rate of 5 slpm. The getter removes electronegative impurities like O_2, H_2O and CO below the 1 ppb level.

Xenon recuperation and storage is possible in a recuperation bottle with a volume of 9.46 liter (2.5 gallons). In order to recuperate the xenon, the bottle is submerged in liquid nitrogen. Because the temperature of liquid nitrogen is lower than the

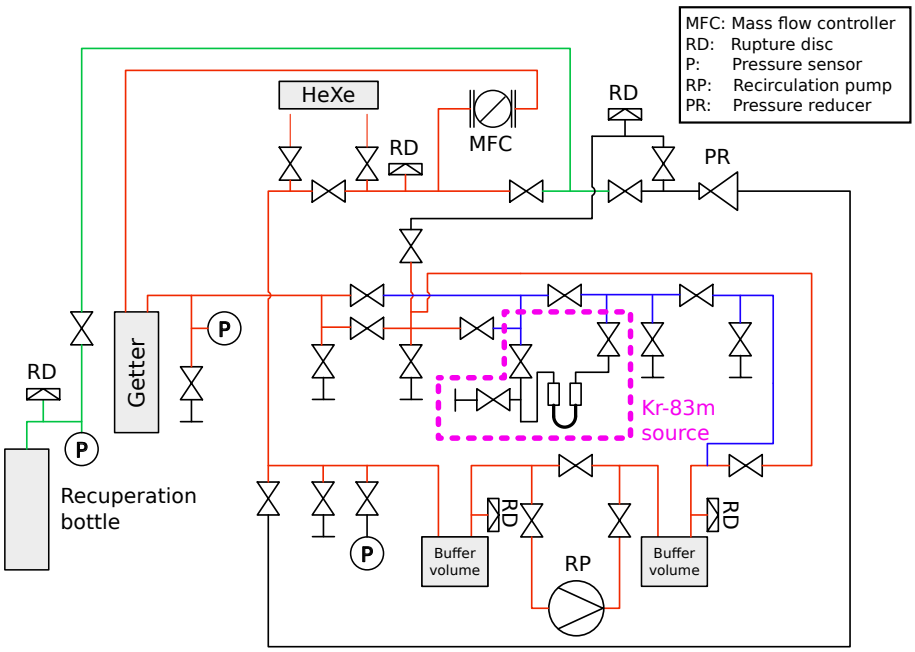

Figure 4.1: Schematic of the HeXe gas system. Colors correspond to the functional parts. **Green:** Recuperation of xenon, **Red:** Recirculation and purification loop and **Blue:** Sampling and source line.

melting point of xenon, xenon freezes out inside the storage bottle. Using this cryo-pumping technique, the xenon can be efficiently removed from the cryostat. The recuperation bottle can withstand an internal pressure of at least 90 bar. At the present stage, it can be used to store the xenon inventory of about 6.5 kg at room temperature. A weight sensor, on which the bottle is suspended, allows to determine the exact amount of xenon present in the storage vessel.

To study the influence of different materials on the purity of the xenon and to introduce calibration sources into the detector, a sampling line is installed in parallel to the main purification loop (Blue in Figure 4.1). It allows to flush through several sample vessels, without interrupting the detector operation. As part of this work, a solid ^{83}Rb source holder was designed and installed on the HeXe gas system. Details on the source are reported in Section 4.3 together with the analysis of first data that was acquired with this source.

4.2.2 The Heidelberg Xenon TPC

In its current version, the detector will host a cylindrical active detection volume with a diameter of 5 cm and 5 cm in height. Two Hamamatsu R6041-406 multichannel PMTs are installed above and below the active volume for detection of the xenon scintillation light.

As in the case of the XENON1T TPC (see Section 1.2), the measurement of a charge induced S2 signal, requires an electric field to drift electrons that are produced by an interaction towards the liquid-gas-interface. The baseline design operates at an electrical field strength of 1 kV/cm, which will be produced using two hexagonal pitched grids (see Figure 4.2). A field for the extraction of electrons from the liquid into the gas phase, will be maintained between the gate electrode and the anode. For this, a voltage of 3.9 kV will be applied on the anode, which is also hexagonal pitched.

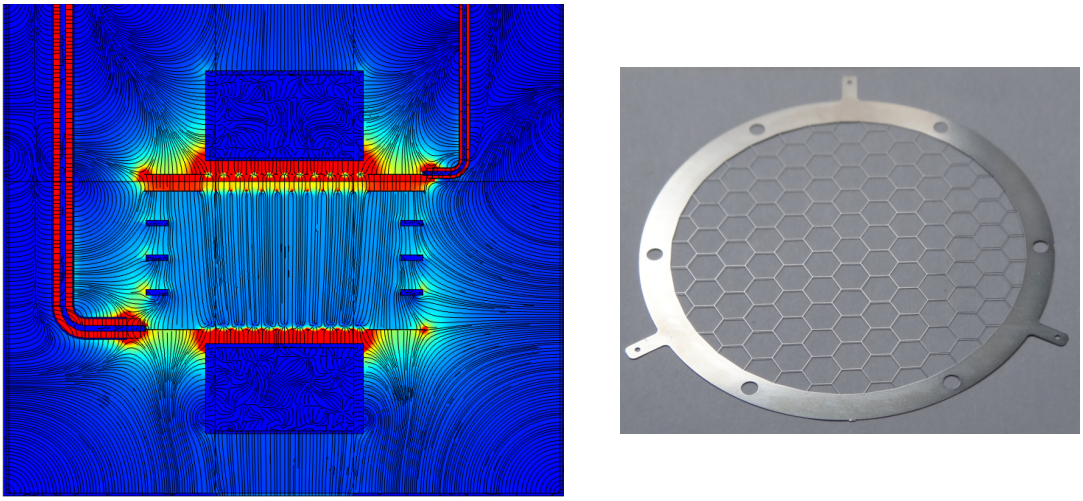

Figure 4.2: **Left:** Simulation of the electric field in the HeXe TPC. Color corresponds to the absolute value of the electric field strength with the lines representing the electrical field lines. Homogeneity of the electric field is ensured by three field shaping rings. Simulation includes the coaxial cables, to connect the cathode and the anode. Figure from [65]. **Right:** Picture of the hexagonal pitched grid, that will be used for cathode, gate and anode.

For a precise reconstruction of the interaction position, it is important that the electric field is homogeneous. Field inhomogeneities will lead to a bent drift path of the electrons, which results in a prolonged drift time. This results into a falsely reconstructed z-coordinate of the event, which in turn is essential to determine the electron lifetime. Therefore, three equidistant field shaping rings with an outer radius of 50 mm, will be placed between the cathode and the gate grid. The high voltage is applied to the field shaping rings, using a resistor chain which is connected between cathode high voltage and ground. The design was optimized for homogeneity of the electric field by an electric field simulation using the commercial finite element software COMSOL [66] (see Figure 4.2).

The detector components are suspended on a Teflon structure (see Figure 4.3). Besides the components mentioned above, it also houses four level meters to measure the height of the liquid level, temperature sensors and an optical fiber allowing

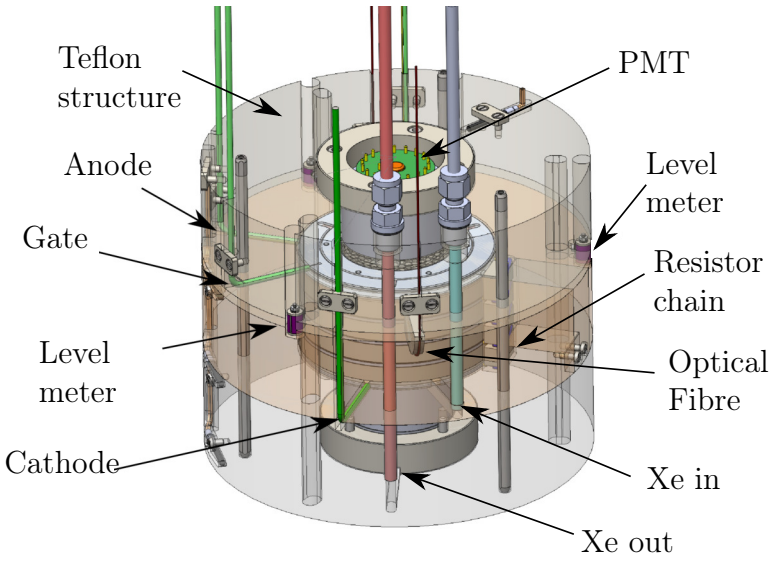

Figure 4.3: Technical drawing of the HeXe time projection chamber.

the gain calibration of the PMTs. Two tubes will be guided into the Teflon. One will be used to fill purified, clean xenon directly inside the active volume, while the other one will serve to extract xenon for purification from below the TPC. It is anticipated, that this leads to an efficient exchange of liquid xenon in the TPC and to a good extraction of impurities from within the active volume.

Thanks to the modular design of the TPC, its drift length can be enlarged at a later stage to a total of 20 cm. By the increased drift time of the electrons in a longer TPC, a higher sensitivity on the electron lifetime can be gained (see Equation 4.1). This will help to study the effects on the xenon purity caused by different materials that are introduced in the TPC.

4.3 Single phase measurement of ^{83m}Kr

The setup for this measurement consists of a Teflon cylinder with a length of 34 cm and 19.6 cm in diameter, that is equipped with two Hamamatsu R11410 PMTs, which are also used in the XENON1T detector. The PMTs were installed above and below a cylindrical active volume of about 7 cm in diameter and 3 cm in height. This setup was already employed in [16] and is shown in Figure 4.4.

Four PT100 temperature sensors were installed along the length of the cylinder. The height of the liquid xenon level inside the detector was then inferred from the temperature decline of these sensors, as soon as they get submerged in the liquid xenon. The 32 mm long level meter, that will be also part of the final TPC setup, was installed above the detection volume and used to verify the complete filling of the detector.

Figure 4.4: Picture of the Teflon block with the two PMTs used for the single phase measurement of ^{83m}Kr. Photograph from C. Föhr

A single phase measurement using a ^{83m}Kr source together with the above setup was done, proving that the system allows safe operation, recirculation and recuperation of liquid xenon. This simpler setup was chosen to test the source that will be used for electron lifetime measurements in the TPC.

4.3.1 Properties of the source

It was shown that metastable krypton is a good calibration source for liquid xenon TPCs [67, 68]. ^{83m}Kr is produced during the electron capture decay of ^{83}Rb which has a half-life of 86.2 days [15]. The source consists of three zeolite beads with a diameter of 2 mm, that have been loaded with an activity of 50 kBq in ^{83}Rb at the Nuclear Physics Institute in Řež. Gaseous ^{83m}Kr diffuses out of the porous zeolite beads and can be dissolved in the xenon recirculation gas stream, that is flushed into the detector. Inside the detector, the metastable krypton decays with a half-life of 1.83 hours [15]. The decay of ^{83m}Kr to the ground state happens subsequently via an intermediate state with a half-life of 154 ns. A conversion electron is emitted by each of the two decays with an energy of 32 keV and 9.4 keV respectively. Figure 4.5 (right) shows a simplified scheme of the ^{83m}Kr decay.

Figure 4.5 (left) shows the holder, that was designed to accommodate the zeolite beads. Three ^{83}Rb loaded beads are enclosed in a U-shaped tube, that is closed off by 0.5 μm particle filters on either side. The particle filters are installed to prevent rubidium from entering the system. This holder was installed on the sampling line of the HeXe gas system (Figure 4.1). The flow through the source was regulated using the bypass valve.

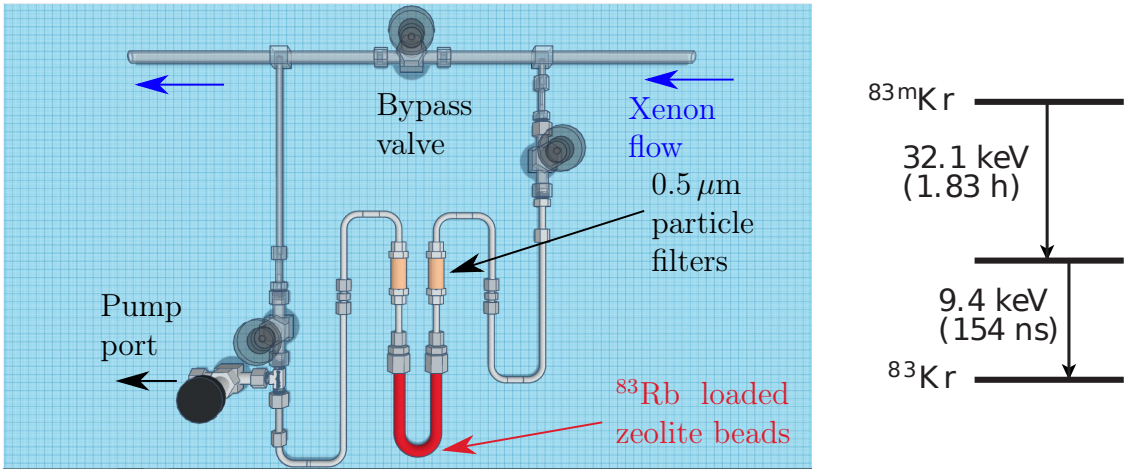

Figure 4.5: **Left:** Source vessel containing the ^{83}Rb loaded zeolite beads (red part). **Right:** Simplified decay scheme of ^{83m}Kr via a short lived intermediate intermediate state under the emission of two conversion electrons [15].

4.3.2 Analysis and results

To judge the presence of krypton within the active volume, the recorded data needs to be analyzed for the appearance of ^{83m}Kr decay events. Due to the time delayed decays of ^{83m}Kr, it provides a signature, that can be clearly identified. In Figure 4.6, a simplified PMT waveform with the typical double peak structure of the decay is shown. The time separation of the two peaks $(t(1) - t(0))$, follows an exponential distribution with a half-life of 154 ns, which is the half-life of the intermediate state of the decay. The areas of the peaks $S(0)$ and $S(1)$, correspond to the amount of energy deposited in the xenon by the two successive decays of ^{83m}Kr. After opening the source, a population of events will appear in the plot of $S(0)$ versus $S(1)$ at the expected signal ratio, over the normally flat background. Since the acquisition window has a length of 4 μs, it is much longer than 154 ns, so both signals are usually contained within one event.

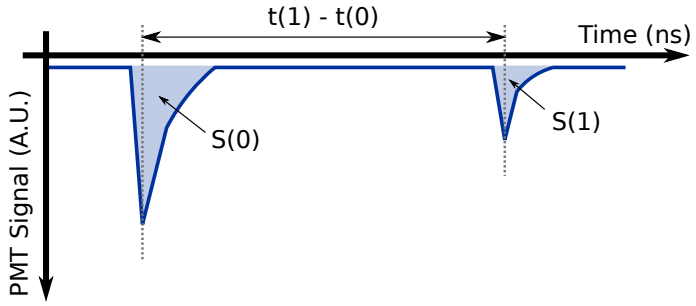

Figure 4.6: Scheme of a PMT waveform showing the typical topology of a ^{83m}Kr decay. Peaks from both time delayed decays are visible. The area of the peaks refers to the deposited energies.

The recorded events were selected according to the following criteria. Both of the two largest peaks had to be detected coincidentally by both PMTs. The largest peak of the event had to occur before the second largest peak (i.e. $t(1) - t(0) > 0$).

Before each measurement, a background data set was recorded.

Measurement in gaseous xenon:

For the first measurement in gaseous xenon at room temperature, the cryostat was filled with a xenon pressure of about 2.3 bar. The source was opened and the circulation flow of 1.4 slpm was redirected through the source vessel. The high voltage of the PMTs was set to −1500 V.

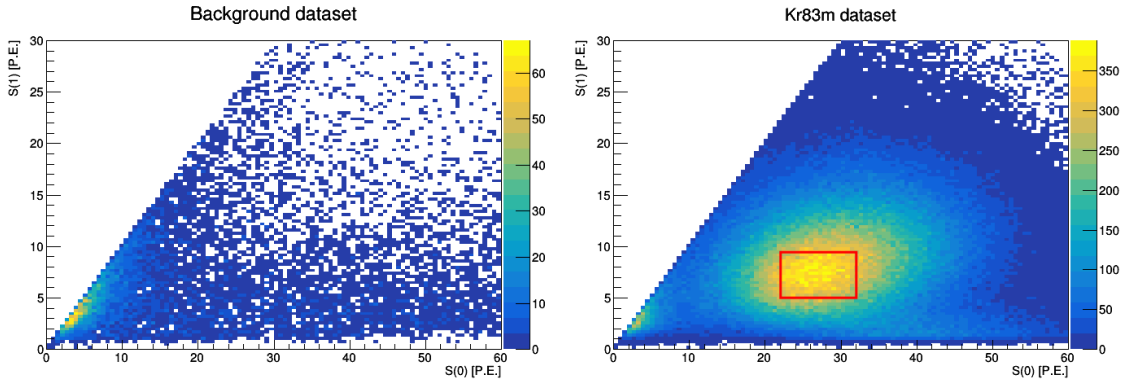

Figure 4.7: **left:** Largest vs. second largest signal for background events. **Right:** Same variables for a measurement with circulation through the ^{83m}Kr source. A population associated to the decay of ^{83m}Kr can be identified.

Figure 4.7 shows the distribution of events in the space of $S(0)$ and $S(1)$ for a background measurement (left) as well as for the ^{83m}Kr data set (right). A population centered at $S(0) = 29\,\text{PE}$ and $S(1) = 7.6\,\text{PE}$ is clearly apparent in the ^{83m}Kr data, whereas in the background measurement no indication for it is visible. In both data sets a population in the low energy region at about 2.5 PE is visible, which might be caused by electronic noise.

For the distribution of the time difference $t(1) - t(0)$, events from the center of the ^{83m}Kr population were selected, as is indicated by the red rectangle. This choice was made to optimize the signal to background ratio. The result as it is shown in Figure 4.8 (right), shows three distinct regions. For time differences between 200 ns to about 1.2 μs, the data is well described by an exponential function with a half-life of (155.5 ± 1.3) ns. The error is determined as the statistical error of the fit, which was constrained to the range from 200 ns to 3 μs. The found half-life is in agreement

with the literature value of 154 ns for the ^{83m}Kr decay. For smaller time differences, the distribution first flattens and then goes to zero. The drop off to zero is probably caused by the decrease of the efficiency, with which the two decay peaks can be separated by the data processor, if they happen very shortly after each other. At time differences above 1.2 μs, the distribution also deviates from the exponential function. One possible reason for this are background events that are still present in the selection. To extract the ^{83m}Kr half-life with less bias due to the flattened part of the distribution, a sum of two exponential functions was used to fit the data. This choice was made, since it described the data better than a constant or a linear function.

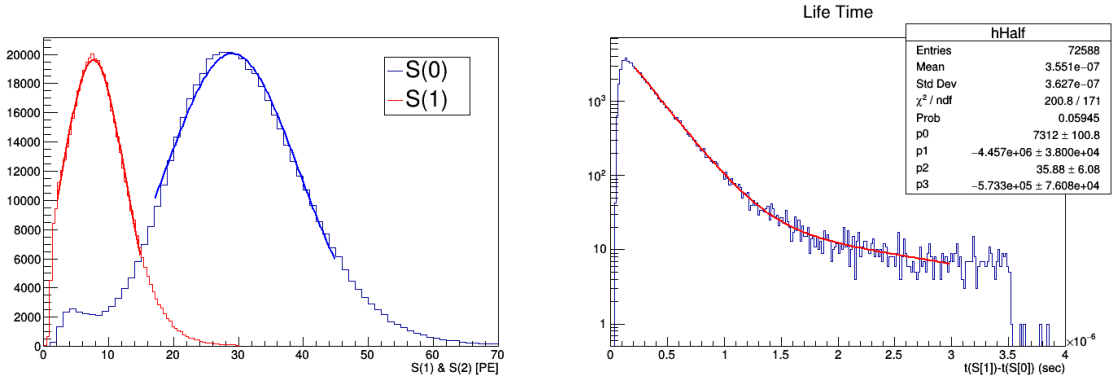

Figure 4.8: **Left:** Spectrum of the area detected in the largest (blue) and second largest (red) peak of each event. Values from the Gaussian fits are reported in Table 4.1. **Right:** Distribution of the time difference between largest and second largest signal. Only events enclosed by the red box shown in the right plot of Figure 4.7 are used. The fitted half-life is in accordance with the literature value (see text).

To determine the mean number of PE (**P**hoto **E**lectrons), detected for each of the two decays, the spectrum of the largest (blue) and second largest (red) peak of the event is plotted and fitted using Gaussian distributions. The result is shown in Figure 4.8 (left) and the fit values are reported in Table 4.1. From the fit values a light yield of about 0.8 PE/keV and 0.9 PE/keV was found for the two decay energies. With an energy resolution of 63% and 34% respectively.

Measurement in liquid xenon

The cryostat was filled with an amount of about 6.5 kg of xenon which was sufficient to cover the active volume completely with liquid xenon. The PMT high voltages for this measurement were set to −1270 V.

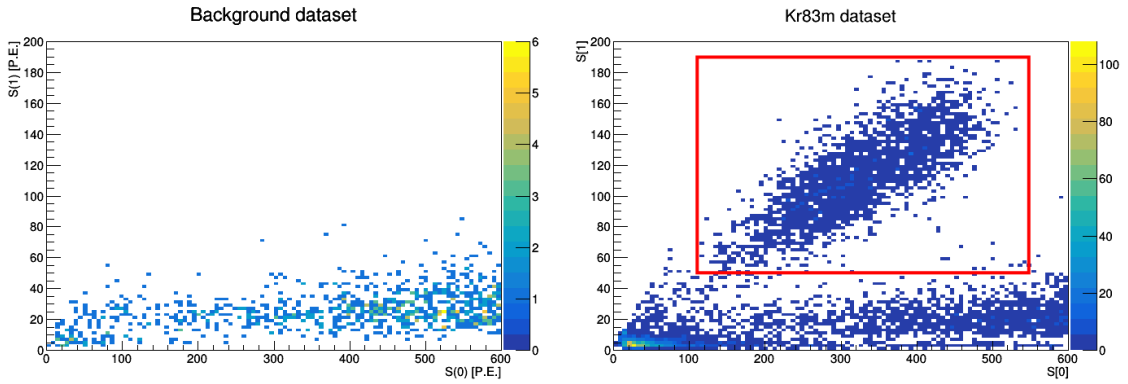

Figure 4.9: Data in liquid xenon: **left:** Largest vs. second largest signal for background events. **Right:** Same variables for a measurement with circulation through the ^{83m}Kr source. A population associated to the decay of ^{83m}Kr can be identified.

Figure 4.9 (right) shows the distribution of events in the space of largest and second largest detected peak for the measurement with the open ^{83m}Kr source. The population, that is centered around $S(0) = 280\,\text{PE}$ and $S(1) = 103\,\text{PE}$ is due to the ^{83m}Kr decay. Figure 4.9 (left) shows the same variables for a background data set recorded in liquid xenon. It can be seen, that the measurement in liquid xenon is much less affected by background events within the region of the ^{83m}Kr population than the measurement that was done in gaseous xenon.

Figure 4.10 (upper left) shows the distribution of the time separation between first and second signal using the events enclosed in the red box. The distribution is well described by a single exponential function with a half-life of $(158.9 \pm 3.8)\,\text{ns}$, which is close to the value given in the literature.

From Figure 4.9 (right) it can be seen, that there is a correlation between the size of $S(0)$ and $S(1)$. A possible explanation for this might be that the efficiency with which the PMTs can detect a light signal, depends on the spatial location within the active volume from which this light signal is emitted. Since the two decay signals from the ^{83m}Kr decay are practically emitted from the same position inside the active volume, the detected signal sizes are correlated. This correlation was reduced by enforcing a condition on the relative amount of light, detected by each of the PMTs. The asymmetry factor A of an event therefore was defined as follows:

$$A = \frac{S_0(0) - S_1(0) + S_0(1) - S_1(1)}{S(0) + S(1)}, \tag{4.3}$$

where $S_0(i)$ corresponds to the contribution of the top PMT to the detected signal of peak i, and $S_1(i)$ is the corresponding contribution of the bottom PMT. $S(i)$ is

the total area of peak i that was detected by both PMTs.

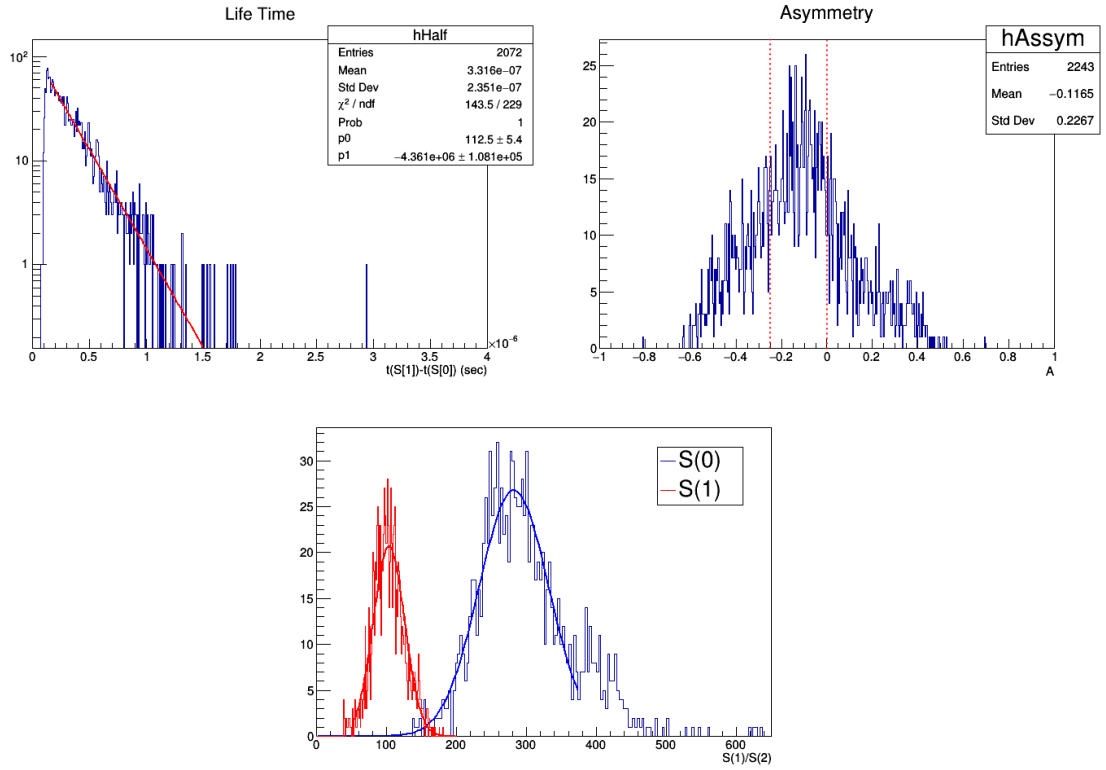

Figure 4.10: **Upper left:** Distribution of the time difference between largest and second largest signal. Only events enclosed by the red box are used. **Upper right:** Asymmetry of the signal detected by upper/lower PMT (see text). **Bottom:** Spectrum of the largest (blue) and second largest (red) peak. Only most central events falling within the red bounds of the asymmetry are used.

The asymmetry distribution of the events, that are enclosed by the box shown in Figure 4.9 (right), is shown in Figure 4.10 (right). The spectrum of the largest (blue) and second largest (red) peak of the event is shown in Figure 4.10 (bottom). For this only the most symmetric events ($-0.25 < A < 0$) were used as is indicated by the red lines in the asymmetry plot. The values resulting from the Gaussian functions, fitted to the two peaks are also reported in Table 4.1. It can be seen, that the light yield for the measurement in liquid xenon is higher than for the measurement in gas. Also worth noting is, that the energy resolution in the liquid measurement is increased with respect to the measurement in gaseous xenon.

Table 4.1: Light yield and its deviation (σ) determined using the ^{83m}Kr decays in liquid and gasous xenon. Values are extred using a Gaussian fit to the two peaks from the ^{83m}Kr decay.

Phase	Decay energy	Mean [PE/keV]	σ[PE/keV]	Resolution (rel.)
Gas	9.4 keV	0.813 ± 0.001	0.514 ± 0.002	63.3%
	32 keV	0.907 ± 0.001	0.313 ± 0.001	34.5%
Liquid	9.4 keV	11.0 ± 0.07	2.40 ± 0.06	21.8%
	32 keV	8.74 ± 0.06	1.51 ± 0.05	17.3%

4.3.3 Discussion and outlook

^{83m}Kr decay events have been observed in gaseous as well as in liquid xenon. The average sizes of the detected signals as can be seen from the obtained fit values, are significantly higher in the liquid phase, than in the gaseous phase. It can be also seen, that the resolution is improved in the liquid phase. This can be understood, by the improved scintillation properties of liquid xenon with respect to gaseous xenon.

Table 4.2 compares the event rate, found within the region of the ^{83m}Kr population, as it is defined by the red rectangles in the Figures 4.7 and 4.9. It is visible that the rate during the liquid measurement was lower, than during the measurement in gaseous xenon. This might hint to an insufficient circulation of liquid xenon within the active volume in the single phase setup.

Table 4.2: Average rate found within the ^{83m}Kr region for measurement in gaseous and liquid xenon.

Phase	Background measurement	^{83m}Kr measurement
Gas	92.5 mHz	6.64 Hz
Liquid	39.2 mHz	784 mHz

As soon as the TPC will be installed, the source can be used for energy calibration and to monitor the electron life-time within the liquid xenon. It can be expected that circulation within the TPC is more efficient due to the tubes, leading into the active volume, which are connected to the purification loop. Therefore the obtainable event rate might be higher compared to the one achieved using the single phase setup. A first measurement of the electron lifetime also requires, that the detected peaks can be classified into light signals (S1) and charge signals (S2). An extension of the data processor will be necessary to provide this functionality.

Summary and discussion

The radon mitigating properties of surface coatings and their potential application in liquid xenon detectors were investigated. The success of an experiment searching for rare events such as in the field of direct dark matter detection might be strongly related to the background level that can be reached. The XENON1T experiment is an example of an experiment whose background is dominated by the ^{222}Rn , emanated from detector materials in contact with xenon.

To measure the ^{220}Rn emanation, a highly sensitive radon monitor based on an electrostatic collection was used. For measurement of ^{222}Rn emanation, highly sensitive, miniaturized proportional counters in combination with a gas line for sample extraction were used, usually applied to screen material for detector construction. This study made use of thoriated tungsten welding rods of 1 mm and 4.8 mm in diameter as a source providing ^{220}Rn and some ^{222}Rn emanation. One sample was also produced by implantation of ^{224}Ra into stainless steel using the recoil from the preceding ^{228}Th decay. In cooperation with the ISOLDE facility, two more stainless steel samples got implanted with ^{226}Ra. They are being investigated for their ^{222}Rn emanation. The result from a gamma spectroscopy verified the presence of ^{226}Ra within the samples.

The coating techniques that were investigated include two physical vapor deposition techniques. Sputtering was investigated in combination with titanium as deposition material. Three samples, consisting of thoriated welding rods with 1 mm in diameter were coated with this technique and addressed for their ^{220}Rn emanation before and after coating. The first sample, consisting of three rods, showed a reduction in ^{220}Rn of 4.5, where the second and third sample, each consisting of five 1 mm welding rods showed significantly lower reduction factors of 1.5 and 1.175 respectively.

Plasma deposition using copper as a coating material was investigated. A first set of samples consisted of three 1 mm thick welding rods, in a second batch one 4.8 mm thick welding rod were coated. Obtained reduction factor in ^{220}Rn was 2.3 for the first sample, and 22.0 for the second sample.

A method for electrodeposition of copper coatings on thoriated tungsten rods was developed. Several samples were produced with ^{220}Rn reduction factors up to about 100. A batch of seven 4.8 mm welding rods which have been coated under controlled conditions, allowed to determine the reduction in ^{222}Rn. A reduction factor of 7.9 was found. Using an ^{224}Ra implanted stainless steel plate, a reduction factor in

^{220}Rn of 12 was found. In a first test addressing the temperature stability of the electrodeposited copper coating layer, a rod coated with a layer about 10 μm thick was submerged in liquid nitrogen ten times. No mechanical damage to the coating was apparent, but a reduction in the ^{220}Rn mitigation might have occured. This case will be further investigated.

The second part of the work was dedicated to the HeXe (**He**idelberg **Xe**non) system, which will soon host a dual-phase liquid xenon TPC. Some of the components of the detector were described and special focus was put on the effect of impurities contained in the liquid xenon. Since this detector is also planned to study how different material introduced into the TPC affects the purity of the xenon, it will be a unique opportunity to study the influence and stability of coating layers under operational conditions of a dual-phase liuid xenon TPC.

A ^{83m}Kr calibration source containing ^{83}Rb loaded zeolite beads was installed on to the HeXe gas system. Two successful measurements with a single-phase setup and using the ^{83m}Kr source were done. In both cases, the decay of metastable krypton via its intermediate state was clearly visible in the data. The extracted half-life was in agreement with values found in the literature for both cases. It was observed, that the measurement in liquid xenon showed a significantly increased light yield and an improved resolution of the two mono energetic ^{83m}Kr decays.

During the measurements, the HeXe gas system, DAQ and slow control proved their capabilities for the next stage of the experiment, that will start with the installation of the TPC. With this, the scientific program will be extended by the possibility to accomplish purity measurements. The detector will therefore also offer the opportunity to investigate the applicability of radon mitigating surface coatings in a dual-phase liquid xenon TPC. If this can be achieved, this would be one further step towards the availability of a valuable new radon mitigation technique suitable for application in liquid xenon detectors.

Part I

Appendix

A Time dependence of ^{212}Po activity

Using the function derived in [30] the in growth of the ^{212}Po activity $A^{ingr}_{212Po}(t)$ can be described. The equilibrium activity A^{eq}_{220Rn} of ^{220}Rn is assumed constant. Due to the short half life of ^{216}Po it can be assumed to be in equilibrium with ^{220}Rn i.e. $A^{eq}_{220Rn} = A^{eq}_{216Po}$ λ_i describes the decay constants of the isotopes in the decay chain ($\lambda_b = \lambda_{212Pb}, \lambda_c = \lambda_{212Bi}, \lambda_d = \lambda_{212Po}$).

$$A^{ingr}_{212Po}(t) = A^{eq}_{216Po}\lambda_d \left(\frac{\lambda_c}{(\lambda_b - \lambda_c)(\lambda_d - \lambda_b)} \left(e^{-\lambda_b t} - e^{-\lambda_c t}\right) + \frac{\lambda_b}{(\lambda_b - \lambda_c)(\lambda_c - \lambda_d)} \left(e^{-\lambda_c t} - e^{\lambda_d t}\right) + \frac{1}{\lambda_d}\left(1 - e^{-\lambda_d t}\right) \right) \tag{A.1}$$

B Electrodeposition parameters

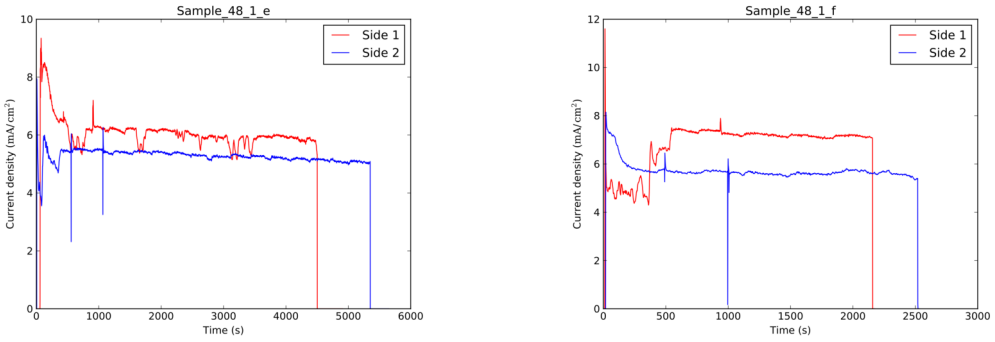

Figure B.1: Surface current density during the electrodeposition of WTh4-2 and WTh4-3. Each rod was coated twice (front and back side).

Table B.1: Mass deposition and estimated layer thicknesses for all rods of all samples. Also quoted are the averaged current densities and the deposition conditions.

Electrode	Δm_{curr} (mg)	Δm_{scale} (mg)	$d_{coating}$ (nm)	U (V)	$\bar{j}$ (A/cm^2)
WTh4-2	243.003	245.9	9661	2.08	5.25
WTh4-3	124.919	126.2	5047	2.1	5.53
WTh5-1-1	123.905	123.45	4939	2.07	6.37
WTh5-1-2	130.74	129.5	5010	2.07	6.24
WTh5-1-3	130.682	132.35	5008	2.07	5.39
WTh5-1-4	130.615	133.5	5005	2.07	5.41
WTh5-1-5	130.578	131.9	5004	2.07	5.74
WTh5-1-6	130.696	131.8	5008	2.07	6.43
WTh5-1-7	130.555	133.0	5003	2.07	5.42
IMP2-1	86.489	89.1	1894	2.58-2.14	5.93
IMP2-2	115.775	119.6	2192	2.58-2.15	6.74

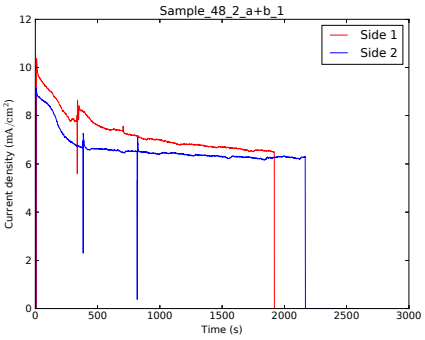
Sample_48_2_a+b_1
Side 1
Side 2
Current density (mA/cm²)
Time (s)

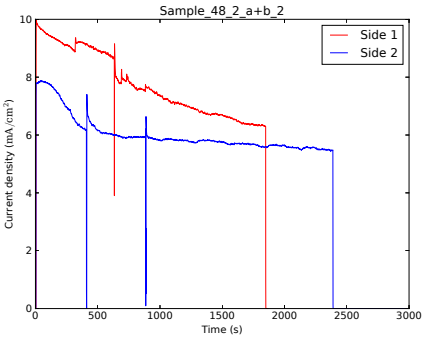
Sample_48_2_a+b_2
Side 1
Side 2
Current density (mA/cm²)
Time (s)

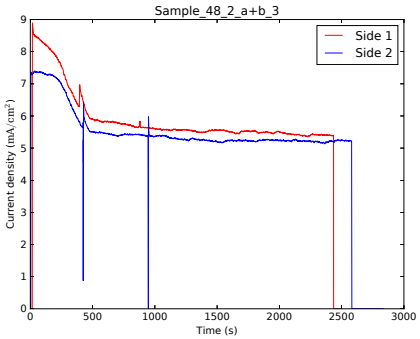
Sample_48_2_a+b_3
Side 1
Side 2
Current density (mA/cm²)
Time (s)

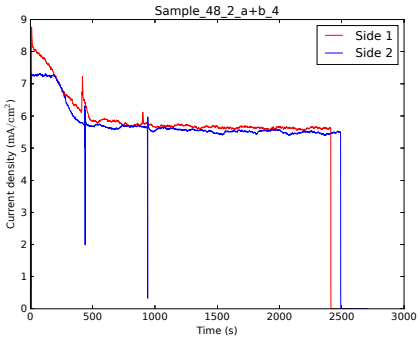
Sample_48_2_a+b_4
Side 1
Side 2
Current density (mA/cm²)
Time (s)

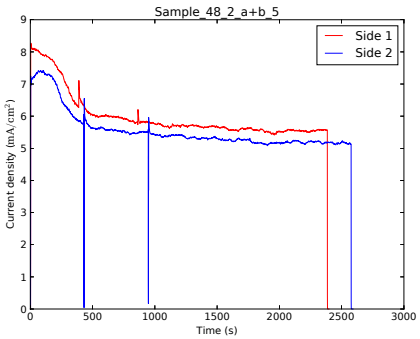
Sample_48_2_a+b_5
Side 1
Side 2
Current density (mA/cm²)
Time (s)

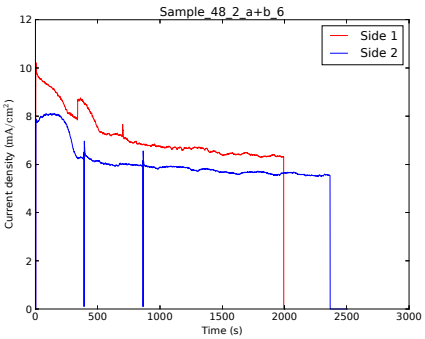
Sample_48_2_a+b_6
Side 1
Side 2
Current density (mA/cm²)
Time (s)

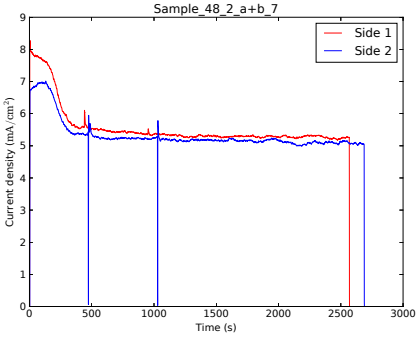

Figure B.2: Surface current density during the electrodeposition of WTh5-1. Each rod was coated twice (front and back side). The first side of the first two electrodes was coated with an electrolyte temperature that was about 10 K higher than usual.

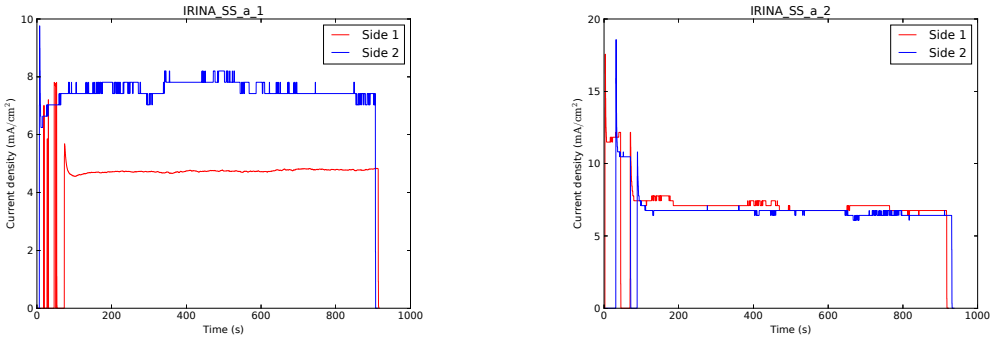

Figure B.3: Surface current density during the electrodeposition of two stainless steel plates (IMP2). Sample was coated twice (front and back side). The technique used a higher voltage for the first 45 sec of the coating followed by a coating where the depositino rate was chosen to be similar to the tungsten examples. For the first plate (side 2) an error in the voltage setting provoked a different deposition. During deposition on the first sample (side 1), the current exeeded the range of the amperemeter in the beginning.

C Error determination

This appendix contains the formulas that were used, to determine the errors on quantities using error propagation.

C.1 Weighted mean

The samples activity A was then determined as the weighted average over the single measurements $\left\{A^{(1)}, A^{(2)}, ..., A^{(n)}\right\}$.

$$A = \sigma_A^2 \sum_{i=1}^{n} \frac{A^{(i)}}{{\sigma^{(i)}}^2} \qquad \text{with} \tag{C.1}$$

$$\sigma_A = \sqrt{\frac{1}{\sum_{i=1}^{n} {\sigma^{(i)}}^{-2}}} \tag{C.2}$$

C.2 Radon reduction factor

Let A_b and σ_{A_b} be the radon activity and its associated standard deviation before coating, while A_a and σ_{A_a} are the respective quantities after coating.

$$\sigma_R = \frac{A_b}{A_a} \sqrt{\left(\frac{\sigma_b}{A_b}\right)^2 + \left(\frac{\sigma_a}{A_a}\right)^2} \tag{C.3}$$

C.3 Systematic correction for thermal emanation

The error on the correction factor σ_R was determined by propagation of the satistical errors of the systematic parameters of the measurement.

$$\sigma_R = R(T_v) \cdot \lambda\tau \sqrt{\left(\frac{\sigma_{V_v}}{V_v}\right)^2 + \left(\frac{\sigma_{Q_s}}{Q_s}\right)^2 + \left(\frac{\sigma_{P_v}}{P_v}\right)^2 + \left(\frac{\sigma_{T_v}}{T_v}\right)^2} \tag{C.4}$$

Where it is assumed, that the decay constant as well as the standard conditions don't have an associated error.

D Systematic parameters of the thermal emanation measurements

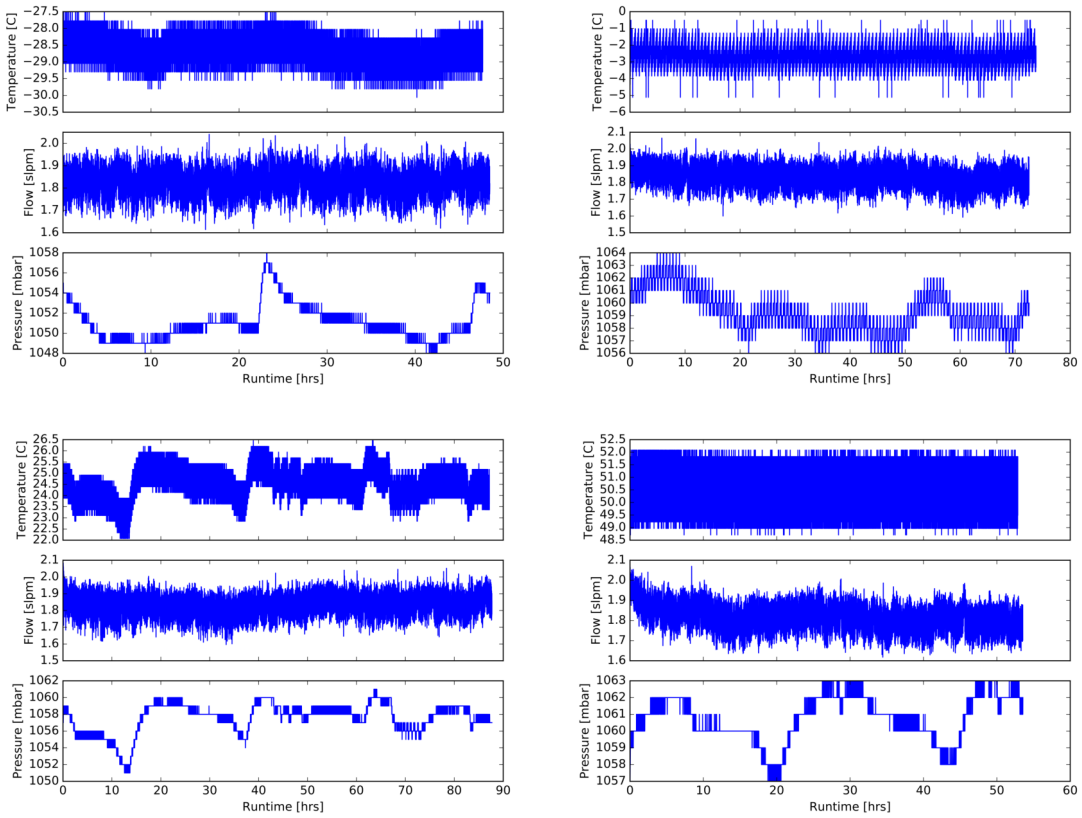

Figure D.1: Systematic parameters of the thermal emanation setup for all measurements

Table D.1: Summary of the mean and standard deviations of the systematic parameters

	1	2	3	4
Temperature ($°C$)	-28.57 ± 0.39	-2.51 ± 0.57	24.65 ± 0.64	50.60 ± 0.67
Flow (sccm)	1828 ± 65	1834 ± 66	1833 ± 66	1819 ± 66
Pressure (mbar)	1051.1 ± 1.8	1059.2 ± 1.6	1057.6 ± 1.8	1060.8 ± 1.4

E Lists

E.1 List of Figures

E.2 List of Tables

F Bibliography

[1] P. A. Ade, N. Aghanim, M. Arnaud, M. Ashdown, J. Aumont, C. Baccigalupi, A. Banday, R. Barreiro, J. Bartlett, N. Bartolo, *et al.*, "Planck 2015 results-xiii. cosmological parameters," *Astronomy & Astrophysics* **594** (2016) A13.

[2] F. Zwicky, "Die rotverschiebung von extragalaktischen nebeln," *Helvetica Physica Acta* **6** (1933) 110–127.

[3] V. Springel, S. D. White, A. Jenkins, C. S. Frenk, N. Yoshida, L. Gao, J. Navarro, R. Thacker, D. Croton, J. Helly, *et al.*, "Simulations of the formation, evolution and clustering of galaxies and quasars," *nature* **435** no. 7042, (2005) 629–636.

[4] M. Taoso, G. Bertone, and A. Masiero, "Dark matter candidates: a ten-point test," *Journal of Cosmology and Astroparticle Physics* **2008** no. 03, (2008) 022.

[5] T. M. Undagoitia and L. Rauch, "Dark matter direct-detection experiments," *Journal of Physics G: Nuclear and Particle Physics* **43** no. 1, (2015) 013001.

[6] V. A. Mitsou, "Overview of searches for dark matter at the lhc," *Journal of Physics: Conference Series* **651** no. 1, (2015) 012023.

[7] V. Vitale, A. Morselli, *et al.*, "Indirect search for dark matter from the center of the milky way with the fermi-large area telescope," *arXiv preprint arXiv:0912.3828* (2009) .

[8] E. Aprile, "The xenon1t dark matter search experiment,". https://doi.org/10.1007/978-94-007-7241-0_14.

[9] E. Aprile, K. Arisaka, F. Arneodo, A. Askin, L. Baudis, A. Behrens, E. Brown, J. Cardoso, B. Choi, D. Cline, S. Fattori, A. Ferella, K. Giboni, A. Kish, C. Lam, R. Lang, K. Lim, J. Lopes, T. M. Undagoitia, Y. Mei, A. M. Fernandez, K. Ni, U. Oberlack, S. Orrigo, E. Pantic, G. Plante, A. Ribeiro, R. Santorelli, J. dos Santos, M. Schumann, P. Shagin, A. Teymourian, E. Tziaferi, H. Wang, and M. Yamashita, "The xenon100 dark matter experiment," *Astroparticle Physics* **35** no. 9, (2012) 573 – 590. http://www.sciencedirect.com/science/article/pii/S0927650512000059.

[10] **XENON** Collaboration, E. Aprile *et al.*, "Physics reach of the XENON1T dark matter experiment," *JCAP* **1604** no. 04, (2016) 027, arXiv:1512.07501 [physics.ins-det].

[11] **XENON** Collaboration, E. Aprile *et al.*, "Material radioassay and selection for the XENON1T dark matter experiment," arXiv:1705.01828 [physics.ins-det].

[12] E. Aprile, J. Aalbers, F. Agostini, M. Alfonsi, F. Amaro, M. Anthony, F. Arneodo, P. Barrow, L. Baudis, B. Bauermeister, *et al.*, "Removing krypton from xenon by cryogenic distillation to the ppq level," *The European Physical Journal C* **77** no. 5, (2017) 275.

[13] **XENON** Collaboration, E. Aprile *et al.*, "First Dark Matter Search Results from the XENON1T Experiment," *Phys. Rev. Lett.* **119** no. 18, (2017) 181301, arXiv:1705.06655 [astro-ph.CO].

[14] S. Lindemann and H. Simgen, "Krypton assay in xenon at the ppq level using a gas chromatographic system and mass spectrometer," *Eur. Phys. J.* **C74** (2014) 2746, arXiv:1308.4806 [physics.ins-det].

[15] S. Chu, L. Ekström, and R. Firestone, "The lund/lbnl nuclear data search, version 2.0, february 1999," 1999. http://nucleardata.nuclear.lu.se/toi/index.asp.

[16] D. Cichon, "Identifying 222rn decay chain events in liquid xenon detectors,".

[17] S. Lindemann, "Intrinsic 85Kr and 222Rn Backgrounds in the XENON Dark Matter Search,".

[18] N. Rupp, "On the detection of 222rn with miniaturized proportional counters: background, sensitivity studies and results for xenon1t,".

[19] E. Aprile, J. Aalbers, F. Agostini, M. Alfonsi, F. Amaro, M. Anthony, F. Arneodo, P. Barrow, L. Baudis, B. Bauermeister, *et al.*, "Online^{222} rn removal by cryogenic distillation in the xenon100 experiment," *The European Physical Journal C* **77** no. 6, (2017) 358.

[20] S. Bruenner, D. Cichon, S. Lindemann, T. M. Undagoitia, and H. Simgen, "Radon depletion in xenon boil-off gas," *The European Physical Journal C* **77** no. 3, (2017) 143.

[21] H. Mehrer, "Diffusion in solids: fundamentals, methods, materials, diffusion-controlled processes,".

[22] P. A. Tipler, R. A. Llewellyn, and G. Czycholl, *Moderne Physik*. Oldenbourg, 2003.

[23] J. F. Ziegler, M. D. Ziegler, and J. P. Biersack, "SRIM - The stopping and range of ions in matter (2010)," *Nuclear Instruments and Methods in Physics Research B* **268** (June, 2010) 1818–1823.

[24] H. Simgen, F. Arnold, H. Aufmhoff, R. Baumann, F. Kaether, S. Lindemann, L. Rauch, H. Schlager, C. Schlosser, and U. Schumann, "Detection of 133 xe from the fukushima nuclear power plant in the upper troposphere above germany," *Journal of environmental radioactivity* **132** (2014) 94–99.

[25] R. Wink, P. Anselmann, D. Dörflinger, W. Hampel, G. Heusser, T. Kirsten, P. Mögel, E. Pernicka, R. Plaga, and C. Schlosser, "The miniaturized proportional counter hd-2 (fe)/(si) for the gallex solar neutrino experiment," *Nuclear Instruments and Methods in Physics Research Section A: Accelerators, Spectrometers, Detectors and Associated Equipment* **329** no. 3, (1993) 541–550.

[26] G. Zuzel and H. Simgen, "High sensitivity radon emanation measurements," *Applied Radiation and Isotopes* **67** no. 5, (2009) 889 – 893. http://www.sciencedirect.com/science/article/pii/S0969804309000608. 5th International Conference on Radionuclide Metrology - Low-Level Radioactivity Measurement Techniques ICRM-LLRMT'08.

[27] P. Pagelkopf and J. Porstendörfer, "Neutralisation rate and the fraction of the positive 218 po-clusters in air," *Atmospheric Environment* **37** no. 8, (2003) 1057–1064.

[28] J. Kiko, "Detector for 222rn measurements in air at the 1mbq/m3 level," *Nuclear Instruments and Methods in Physics Research Section A: Accelerators, Spectrometers, Detectors and Associated Equipment* **460** no. 2, (2001) 272 – 277. http://www.sciencedirect.com/science/article/pii/S0168900200010822.

[29] T. Skwarnicki, *A study of the radiative CASCADE transitions between the Upsilon-Prime and Upsilon resonances*. PhD thesis, Cracow, INP, 1986. http://www-library.desy.de/cgi-bin/showprep.pl?DESY-F31-86-02.

[30] L. Fischer, "Investigation of material coatings in order to reduce the emanation of radon,".

[31] W. Maneschg, M. Laubenstein, D. Budjáš, W. Hampel, G. Heusser, K. Knöpfle, B. Schwingenheuer, and H. Simgen, "Measurements of extremely low radioactivity levels in stainless steel for gerda," *Nuclear Instruments and Methods in Physics Research Section A: Accelerators, Spectrometers, Detectors and Associated Equipment* **593** no. 3, (2008) 448 – 453. http://www.sciencedirect.com/science/article/pii/S0168900208007833.

[32] N. R. Commission *et al.*, "Systematic radiological assessment of exemptions for source and byproduct materials," *Washington, DC: US NRC* (2001) . https://www.nrc.gov/reading-rm/doc-collections/nuregs/staff/sr1717/nureg-1717.pdf.

[33] S. Lindemann, "Reinigung und nachweis von edelgasen mit miniaturisierten proportionalzählrohren,".

[34] D. Forkel-Wirth, "Exploring solid state physics properties with radioactive isotopes," *Reports on Progress in Physics* **62** no. 4, (1999) 527. http://stacks.iop.org/0034-4885/62/i=4/a=002.

[35] J. C. Cornell, "Radioactive ion beam facilities in Europe: Current status and future development,".

[36] H.-J. Kluge *et al.*, *ISOLDE users' guide*, vol. 86. CERN, 1986. http://cds.cern.ch/record/170359/files/CERN-86-05.pdf.

[37] P. Van Duppen and K. Riisager, "Physics with rex-isolde: from experiment to facility," *Journal of Physics G: Nuclear and Particle Physics* **38** no. 2, (2011) 024005. https://hal.archives-ouvertes.fr/hal-00600873/document.

[38] E. Kugler, "The isolde facility at the cern ps booster," *Nuclear Instruments and Methods in Physics Research Section B: Beam Interactions with Materials and Atoms* **79** no. 1-4, (1993) 322–325. http://cds.cern.ch/record/247918/files/cer-000164119.pdf.

[39] E. Kugler, D. Fiander, B. Johnson, H. Haas, A. Przewloka, H. Ravn, D. Simon, K. Zimmer, I. Collaboration, *et al.*, "The new cern-isolde on-line mass-separator facility at the ps-booster," *Nuclear Instruments and Methods in Physics Research Section B: Beam Interactions with Materials and Atoms* **70** no. 1-4, (1992) 41–49.

[40] S. Swann, "Magnetron sputtering," *Physics in technology* **19** no. 2, (1988) 67.

[41] S. Gopikishan, I. Banerjee, and S. Mahapatra, "Influence of magnetic field on plasma parameters and thin film deposition along axial and radial distances in dc magnetron," *arXiv preprint arXiv:1704.06503* (2017) .

[42] M. Gee, A. Gant, I. Hutchings, R. Bethke, K. Schiffman, K. V. Acker, S. Poulat, Y. Gachon, and J. von Stebut, "Progress towards standardisation of ball cratering," *Wear* **255** no. 1, (2003) 1 – 13. http://www.sciencedirect.com/science/article/pii/S0043164803000917. 14th International Conference on Wear of Materials.

[43] J. A. Thornton, "High rate thick film growth," *Annual review of materials science* **7** no. 1, (1977) 239–260.

[44] K. von Niessen and M. Gindrat, "Plasma spray-pvd: A new thermal spray process to deposit out of the vapor phase," *Journal of Thermal Spray Technology* **20** no. 4, (Jun, 2011) 736–743. https://doi.org/10.1007/s11666-011-9654-9.

[45] F. S. T. FST, "https://www.fst.nl/systems/aps-plasma-thermal-spray-coating-system/,".

[46] C. Wang, J. Lei, C. Bjelkevig, S. Rudenja, N. Magtoto, and J. Kelber, "Electrodeposition of adherent copper film on unmodified tungsten," *Thin Solid Films* **445** no. 1, (2003) 72 – 79. http://www.sciencedirect.com/science/article/pii/S0040609003012392.

[47] A. Ibañez and E. Fatás, "Mechanical and structural properties of electrodeposited copper and their relation with the electrodeposition parameters," *Surface and Coatings Technology* **191** no. 1, (2005) 7 – 16. http://www.sciencedirect.com/science/article/pii/S0257897204003366.

[48] J. Goldstein, *Practical scanning electron microscopy: electron and ion microprobe analysis*. Springer Science & Business Media, 2012.

[49] K. Mittal, "Adhesion measurement of thin films," *Active and Passive Electronic Components* **3** no. 1, (1976) 21–42.

[50] A. Technologies, "Agilent laser and optics user's manual volume i fifth part,". http://www.uzimex.cz/soubory/20080403_laser_optika_cast_1.pdf.

[51] F. Cverna, "Thermal properties of metals," *ASM International, Materials Park, OH* (2002) .

[52] F. Sensor, "Mass flow versus volumetric flow,". https://www.first-sensor.com/cms/upload/appnotes/AN_Massflow_E_11153.pdf.

[53] M. Jiranek and Z. Svoboda, "Transient radon diffusion through radon-proof membranes: A new technique for more precise determination of the radon diffusion coefficient," *Building and Environment* **44** no. 6, (2009) 1318–1327.

[54] M. Wojcik, W. Wlazło, G. Zuzel, and G. Heusser, "Radon diffusion through polymer membranes used in the solar neutrino experiment borexino," *Nuclear Instruments and Methods in Physics Research Section A: Accelerators, Spectrometers, Detectors and Associated Equipment* **449** no. 1, (2000) 158–171.

[55] D. Iskandar, H. Yamazawa, and T. Iida, "Quantification of the dependency of radon emanation power on soil temperature," *Applied Radiation and Isotopes* **60** no. 6, (2004) 971 – 973. http://www.sciencedirect.com/science/article/pii/S0969804304000442.

[56] K. Y. Lee, S. Y. Cho, Y. Y. Yoon, and Y. N. Jang, "Determination of the radon emanation fraction from phosphogypsum using lsc," *Journal of Radioanalytical and Nuclear Chemistry* **291** no. 1, (Jan, 2012) 197–200. https://doi.org/10.1007/s10967-011-1306-5.

[57] G. J. Schrobilgen, "radon (rn)," *Encyclopaedia Britannica* (2014) .

[58] A. Dobi, D. Leonard, C. Hall, L. Kaufman, T. Langford, S. Slutsky, and Y.-R. Yen, "Study of a zirconium getter for purification of xenon gas," *Nuclear Instruments and Methods in Physics Research Section A: Accelerators, Spectrometers, Detectors and Associated Equipment* **620** no. 2, (2010) 594–598.

[59] E. Aprile and T. Doke, "Liquid xenon detectors for particle physics and astrophysics," *Reviews of Modern Physics* **82** no. 3, (2010) 2053.

[60] E. Aprile, *Noble gas detectors*. John Wiley & Sons, 2006.

[61] J. Jortner, L. Meyer, S. A. Rice, and E. Wilson, "Localized excitations in condensed ne, ar, kr, and xe," *The Journal of chemical physics* **42** no. 12, (1965) 4250–4253.

[62] S. A. Brünner, "Mitigation of 222rn induced background in the xenon1t dark matter experiment,".

[63] K. Neuberger GmbH, *Diaphragm-Gas Sampling Pumps with double diaphragm System (user manual)*. 2014.

[64] SAES, "Ps4-mt3/15-r/n specifications (user manual),". http://www.saespuregas.com/Library/documents/s110-243_rev__528.pdf.

[65] G. Eurin, "Internal communication,".

[66] C. Multiphysics, "Introduction to comsol multiphysics®," *URL: https://cdn. comsol. com/documentation/5.2* **1** (1998) .

[67] L. Kastens, S. Cahn, A. Manzur, and D. McKinsey, "Calibration of a liquid xenon detector with kr 83 m," *Physical Review C* **80** no. 4, (2009) 045809.

[68] A. Manalaysay, T. M. Undagoitia, A. Askin, L. Baudis, A. Behrens, A. Ferella, A. Kish, O. Lebeda, R. Santorelli, D. Vénos, *et al.*, "Spatially uniform calibration of a liquid xenon detector at low energies using k 83 mr," *Review of Scientific Instruments* **81** no. 7, (2010) 073303.

Acknowledgments

At this point I want to thank everyone who made this work possible. First, I want to thank Prof. Manfred Lindner, for giving me the opportunity to work out my thesis within the XENON group at the Max-Planck-Institut für Kernphysik. I also want to thank Prof. Stephanie Hansmann-Menzemer for reviewing it as second referee.

During the last year, Dr. Hardy Simgen patiently and gratefully shared his thoughts and experience with me. I owe him big thank for his support which proofed to be essential for the successful completion of my work. I am also very grateful for the support I received by Dr. Teresa Marrodan. Her coordination and advice is invaluable not only for the success of the HeXe project but was also essential for the progress of my analysis. Alongside she provided me with valuable comments and suggestions for my thesis.

I like to thank all my colleagues at the MPIK for the pleasant and encouraging working atmosphere. Especially I want to emphasize the support and guidance I received by Dr. Guillaume Eurin. Throughout the last year we closely worked together in an open and always friendly manner. In many discussions, I was given the chance to express my own opinion and bring in my own ideas. Until the very end he provided me with comments and corrections for my work. This improved my writing abilities and the quality of my work significantly. I also want to thank Dr. Stefan Brünner for the useful discussions we had, as well as Dr. Constanze Hasterock. Both provided me with helpful comments and corrections to my thesis.

Professor Klaus Blaum I want to thank for supporting us during the production of the radium implanted steel samples. Alongside I want to thank Dr. Karl Johnston, Dr. Juliana Schell as well as their colleagues from ISOLDE at CERN who made this possible. The Federal Ministry of Education and Research (BMBF) through contract 05K13TSA and 05K16PGA is acknowledged for equipment used during the implantation. Dr. Jochen Schreiner I want to thank for his help during the preparation of the ^{83m}Kr source as well as for taking care of all the formalities necessary to receive and ship the samples that were used in this work. I would also like to thank Benjamin Gramlich who helped me with the electro deposition procedure and Jonas Westermann who performed the measurements using the miniaturized proportional counters. Last I would like to thank my family and my friends. Throughout my studies they were always there to support me and never doubted that I will succeed.

Erklärung:

Ich versichere, dass ich diese Arbeit selbstständig verfasst habe und keine anderen als die angegebenen Quellen und Hilfsmittel benutzt habe.

Heidelberg, den (Datum) .....